

# A generalised sigmoid population growth model with energy dependence: application to quantify the tipping point for Antarctic shallow seabed algae

Elise Mills<sup>a,b,c,\*</sup>, Graeme F. Clark<sup>d,e,f</sup>, Matthew J. Simpson<sup>b</sup>, Mark Baird<sup>g</sup>, Matthew P. Adams<sup>a,b,c,h</sup>

<sup>a</sup>*Securing Antarctica's Environmental Future, Queensland University of Technology, Brisbane, 4001, QLD, Australia*

<sup>b</sup>*School of Mathematical Sciences, Queensland University of Technology, Brisbane, 4000, QLD, Australia*

<sup>c</sup>*Centre for Data Science, Queensland University of Technology, Brisbane, 4000, QLD, Australia*

<sup>d</sup>*Evolution & Ecology Research Centre, University of New South Wales, Sydney, 2052, NSW, Australia*

<sup>e</sup>*Centre of Marine Science and Innovation, University of New South Wales, Sydney, 2052, NSW, Australia*

<sup>f</sup>*School of Life and Environmental Sciences, University of Sydney, Camperdown, 2006, NSW, Australia*

<sup>g</sup>*CSIRO Oceans and Atmosphere, Hobart, 7001, TAS, Australia*

<sup>h</sup>*School of Chemical Engineering, The University of Queensland, St Lucia, 4072, QLD, Australia*

---

## Abstract

Sigmoid growth models are often used to study population dynamics. The size of a population at equilibrium commonly depends explicitly on the availability of resources, such as an energy or nutrient source, which is not explicit in standard sigmoid growth models. A simple generalised extension of sigmoid growth models is introduced that can explicitly account for this resource-dependence, demonstrated by three examples of this family of models of increasing mathematical complexity. Each model is calibrated and compared to observed data for algae under sea-ice in Antarctic coastal waters. It was found that through careful construction, models satisfying the proposed framework can estimate key properties of a sea-ice break-out controlled tipping point for the algae, which cannot be estimated using standard sigmoid growth models. The proposed broader family of energy-dependent sigmoid growth models likely has usage in many population growth contexts where resources limit population size.

*Keywords:* Bayesian inference, Logistic growth, Model-data calibration, Regime shift, Sequential

---

\*Corresponding Author

*Email addresses:* [elise.mills@qut.edu.au](mailto:elise.mills@qut.edu.au) (Elise Mills), [graeme.clark@sydney.edu.au](mailto:graeme.clark@sydney.edu.au) (Graeme F. Clark), [matthew.simpson@qut.edu.au](mailto:matthew.simpson@qut.edu.au) (Matthew J. Simpson), [mark.baird@csiro.au](mailto:mark.baird@csiro.au) (Mark Baird), [mp.adams@qut.edu.au](mailto:mp.adams@qut.edu.au) (Matthew P. Adams)

## 1. Introduction

Systems with a dependence on the availability of resources, such as an energy or nutrient source, are ubiquitous in population biology across all flora and fauna: for example, the dependence of plant growth on available light, including minimum light requirements (Erfteimeijer and Robin Lewis, 2006), and the dependence of human health on energy intake, including minimum food intake requirements (World Health Organization et al., 2004). With this in mind, we note that many real systems require a steady state population size  $N^* > 0$  only when an external forcing beneficial to the system, generically here referred to as ‘energy’  $E$ , is above a minimum threshold value, known as a ‘compensation’ value  $E_c$ , and  $N^* = 0$  if these energetic requirements are not met. This is a property that commonly used growth models are unable, without modification, to account for.

For example, classical sigmoid growth models, such as the logistic growth model and two alternatives to that model, the Gompertz and Richards’ models (Tsoularis and Wallace, 2002), have found wide application across multiple disciplines. These models’ applications range from biology and ecology, for example modelling populations (Murray, 1989), leaf area growth (Thornley, 1990) and forest recovery (Acevedo et al., 2012), to modelling systems in other fields, such as the market penetration of new products (Fisher and Pry, 1971). The desired application generally guides the choice of model (Simpson et al., 2022), with the key differences of each model occurring at larger densities (Browning et al., 2017). The basic frameworks of such models and their associated phenomena have been discussed extensively elsewhere (Banks, 1993). To summarise, a general sigmoid growth model takes the form:

$$\frac{dN}{dt} = rN(t) f_c(N(t); K, \lambda), \quad (1)$$

where  $r > 0$  is the growth rate,  $N(t) \geq 0$  is the population size,  $t \geq 0$  is time and  $f_c(N(t); K, \lambda) \geq 0$  is a non-dimensional ‘crowding’ function, with carrying capacity  $K$  and other parameters  $\lambda$  (where relevant), that influences the population’s net growth rate (Jin et al., 2016), where typically

$f_c(K; K, \lambda) = 0$ . These crowding functions take on the following typical forms, which are governed by the specific model being used:

$$f_c(N(t); K) = 1 - \frac{N(t)}{K} \quad (\text{Logistic growth}) \quad (2a)$$

$$f_c(N(t); K, \beta) = 1 - \left(\frac{N(t)}{K}\right)^\beta \quad (\text{Richards' growth}) \quad (2b)$$

$$f_c(N(t); K) = \log\left(\frac{K}{N(t)}\right) \quad (\text{Gompertz growth}) \quad (2c)$$

where  $K > 0$  (and  $\beta > 0$  when present, as the only member of additional parameters  $\lambda$ ). The crowding functions listed in Equation (2) result in the stable steady state  $N^* = K$  and the unstable steady state  $N^* = 0$ . Sigmoid growth models with logistic and Richards' crowding functions are characterised by approximately exponential growth  $dN(t)/dt \approx rN(t)$  for small populations ( $N(t) \ll K$ ), and for all crowding functions the growth decreasing to zero as the population size approaches the carrying capacity ( $N(t) \rightarrow K^-$ ) due to increasing resource limitation (Murray, 1989). The stability of  $N^* = K$  means that as long as the initial population size is greater than zero,  $N(t) \rightarrow K^-$  as  $t \rightarrow \infty$  (Murray, 1989).

Richer and more nuanced population behaviours arise through strategic modifications of Equation (1). For example, the effect of the crowding function reducing growth as  $N(t) > 0$  increases towards  $K$  (Jin et al., 2016) can be partially countered by modifying Equation (1) with a weak Allee effect (Allee and Bowen, 1932; Wang et al., 2002; Taylor and Hastings, 2005; Fadai and Simpson, 2020):

$$\frac{dN}{dt} = rN(t)f_c(N(t); K, \lambda) \left(1 + \frac{N(t)}{C}\right), \quad (3)$$

where  $C > 0$  is a positive constant. This modification changes the magnitude of  $dN(t)/dt$ , but does not alter its steady state behaviour.

Alternatively, Equation (1) can be modified so that  $N^* = 0$  and  $N^* = K$  are *both* stable steady states, via introduction of a strong Allee effect (Allee and Bowen, 1932; Wang et al., 2002; Taylor

and Hastings, 2005; Fadai and Simpson, 2020):

$$\frac{dN}{dt} = rN(t)f_c(N(t); K, \lambda) \left( \frac{N(t)}{D} - 1 \right), \quad (4)$$

where  $D > 0$  is a positive constant. The concept of a second stable steady state is an example of bistability (Holling, 1973; Noy-Meir, 1975).

The models discussed thus far only permit  $N^* = 0$  and/or  $N^* = K$  as stable steady states. However, in practice, populations may stabilise at population sizes or abundances that depend on external forcing; for example,  $N^*$  may gradually increase with environmental suitability, and/or  $N^*$  may gradually decrease with environmental stress. Additional modifications to Equation (1) are required to simulate this behaviour.

One approach to obtain  $N^* \neq 0, K$  is the introduction of limiting or harvesting terms, which describe the removal of portions of a population (Brauer and Sánchez, 1975; Brauer, 1979), for example, the effects of fishing on a fish population (Murray, 1989). Such a term can be constant or variable depending on, for example, time (Idlango et al., 2017) or density (Cooke and Witten, 1986), and is incorporated as shown in Equation (5) for a time-dependent harvesting term  $H(t)$ :

$$\frac{dN(t)}{dt} = rN(t) f_c(N(t); K, \lambda) - H(t), \quad (5)$$

where it is typically assumed that  $H(t) \geq 0$ . For example, consider the application of the harvesting term to the logistic model:

$$\frac{dN(t)}{dt} = rN(t) \left( 1 - \frac{N(t)}{K} \right) - H(t). \quad (6)$$

Setting  $H(t) = H_0N(t)$ , for some constant  $H_0 > 0$ , changes the model's dynamics so that the stable steady state is  $N^* = K(1 - H_0/r)$  if  $H_0 < r$ , and the stable steady state is  $N^* = 0$  if  $H_0 > r$ . Thus, the stable steady state of the population  $N^*$  decreases as the per-capita harvesting constant  $H_0$  increases. Different steady state behaviour can arise from different choices of  $H(t)$ , although this behaviour may not be obvious or apparent directly from Equation (6) without additional derivations.

To the same end, other works (Grozdanovski et al., 2009; Idlango et al., 2012; Shepherd et al., 2012; Idlango et al., 2017) consider sigmoid growth models with  $r$  and  $K$  as functions of time,  $r(t)$  and  $K(t)$ :

$$\frac{dN(t)}{dt} = r(t)N(t) f_c(N(t); K(t), \lambda). \quad (7)$$

Such modifications allow the incorporation of more dynamic effects, such as responses of the population to background seasonality (Grozdanovski et al., 2009). Although these modifications do take into account environmental factors, the only allowed steady states are  $N^* = 0$  or the quasi-steady state  $N = K(t)$  (or within a small neighbourhood of  $N = K(t)$  (Idlango et al., 2012; Shepherd et al., 2012; Idlango et al., 2017)) with no possibility of  $0 < N^* \ll K$ .

One potential application of Equation (7) is to treat the growth rate  $r(t)$  and/or the carrying capacity  $K(t)$  as functions of an external forcing that is permitted to be time-varying. If this external forcing is detrimental to the population, the resulting effects may be similar to that of the harvesting rate in Equation (5); we have not yet dealt with the case where the external forcing is beneficial to the population. In the case of a beneficial external forcing, we may require, for example, that  $N^* > 0$  only when a relevantly defined quantity of energy  $E$  exceeds some compensation value  $E_c$ , and  $N^* = 0$  if this energy requirement is not met (i.e. if  $E < E_c$ ). In ecological situations, a limiting resource or energy  $E$  can be time-dependent ( $E(t)$ ), but we will limit our considerations here to examples where energy  $E$  is constant over time.

A naive modification of Equation (7) to capture energy dependence satisfying the above requirements ( $N^* > 0$  when  $E > E_c$ ,  $N^* = 0$  when  $E < E_c$ ) is to choose  $K(E)$  and  $r(E)$  to both be monotonically non-decreasing (i.e. either static or increasing) functions of  $E$ , such that  $K(E_c) = 0$ ,  $r(E_c) = 0$ , and:

$$\lim_{E \rightarrow E_c} \left[ r(E) f_c(N(t); K(E), \lambda) \right] = 0, \quad (8)$$

with this latter condition required to avoid singularity in  $dN/dt$  when  $E = E_c$ . For example, for logistic growth, Equation (8) requires  $\lim_{E \rightarrow E_c} r(E)$  to approach zero faster than  $\lim_{E \rightarrow E_c} K(E)$  to avoid singularity. Equation (8) is thus a mathematical inconvenience that could also yield non-realistic behaviour for  $dN/dt$  in the vicinity of  $E = E_c$  if  $r(E)$  and  $K(E)$  are not chosen carefully.

An alternative inelegant approach to modelling energy dependence is to use Equation (6), noting that  $H(t) = H_0 N(t)$  permits a smooth transition from  $N^* = 0$  when  $H_0 > r$  to  $N^* = K(1 - H_0/r)$  when  $H_0 < r$ , but only if  $H_0$  is interpreted as an environmental stress (i.e. conceptually the opposite of the energy dependence we wish to capture). If we wish for the model to capture steady state population behaviour that has energy dependence, the structure of Equation (6) does not intuitively capture this concept.

One application where growth models that capture energy dependence may be of great use is benthic ecosystems in the coastal waters of Antarctica. Antarctic benthic ecosystems play an important role in many global cycles (Murphy et al., 2021); however there are many challenges faced when attempting to model these ecosystems (Kennicutt et al., 2014). Critically, detailed long-term data is often not available (Convey et al., 2014; Koerich et al., 2023), driving the need for modelling that incorporates ecological processes (Koerich et al., 2023) or environmental conditions, such as light availability.

Coastal waters surrounding Antarctica are subject to highly seasonal variation in sea-ice cover, the presence of which restricts the transmission of light to the benthic environment below (Katlein et al., 2015; Clark et al., 2017). The total time period of sea-ice cover per year in Antarctic waters is generally decreasing (Abram et al., 2010; Stammerjohn et al., 2012), and models predict decreases in the extent of sea-ice into the future (Mayewski et al., 2009). These processes result in an increase in the amount of light per year reaching the benthic ecosystems, an effect exacerbated by the non-linear relationship between the timing of sea-ice break-out and annual light dose (Runcie and Riddle, 2006; Clark et al., 2013a). More specifically, the light dose per day depends on what day of the year it is – as both the day length and height of the Sun in the sky determines the daily light dose; this yields non-linearity in the relationship between the timing of sea-ice break-out and annual light dose.

The total time period of sea-ice cover each year has a heavy influence on Antarctic shallow-water marine ecosystems, whose composition is determined by the amount of light received (Miller and Etter, 2008; Clark et al., 2017). These ecosystems are home to a diverse number of species (Griffiths, 2010), with a high level of endemism (i.e. species uniqueness) (Dell, 1972; Clayton,

1994; Peck, 2018). The presence of sea-ice creates a dark and calm environment which favours habitation by macroinvertebrate communities (Picken, 1985; Clayton, 1994; Clark et al., 2013a, 2015). However, should the period of sea-ice cover decrease to the extent that the ecosystem is receiving sufficient light to allow algae growth, the algae will outcompete invertebrates, resulting in a tipping point where endemic invertebrate communities are replaced with beds of macroalgae (Clark et al., 2013a). Such trends have already been observed in the Arctic (Kortsch et al., 2012; Krause-Jensen et al., 2012; Scherrer et al., 2019) and Antarctic (Quartino et al., 2013), and pose a significant risk to the survival of invertebrate communities and thus the biodiversity of the Antarctic continent’s shallow-water benthic zone. To the best of our knowledge, these ecosystems are the only Antarctic ecosystems assessed by the International Union for Conservation of Nature Red List of Ecosystems (IUCN RLE) for their collapse threat status (Clark et al., 2015; IUCN-CEM, 2022), having been classified as ranging from Near Threatened to Vulnerable, and are at further risk due to record low sea-ice coverage in 2023 (Purich and Doddridge, 2023).

In this work, we introduce a generalised sigmoid population growth model framework that intuitively captures energy dependence of the steady state population. The family of models we introduce is a straightforward extension of sigmoid population growth models that can capture a wide range of possible functional forms. These models guarantee a steady state population of  $N^* = 0$  when the available energy  $E$  is less than a threshold value ( $E_c$ ), and a steady state population that is a non-decreasing function of  $E$  when  $E$  is above the threshold value  $E_c$ . We present and analyse three examples of this model family, of increasing complexity and relevance.

We apply and calibrate the three example models to a case study involving data collected for Antarctic shallow water benthic communities (Clark et al., 2013a) at one time point per community; this data describes the balance between algae and invertebrate populations (discussed in detail in Section 2.2.1). We compare the merits of our proposed energy-dependent models for forecasting algae cover in response to available light, and for predicting tipping points and other key ecological parameters in benthic algae-invertebrate ecosystems where light availability is restricted by sea-ice cover.

The case study is an example of a system in which changes in the abundance of these energy

resources beyond a critical threshold, or ‘tipping point’, can result in sudden and widespread change of the system to an alternative state (Scheffer et al., 2001). However, more broadly, the presented models are sufficiently general that they can represent the dynamics of any system in which there is nontrivial dependence of a steady state population on available energy resources (for example nutrients, light, prey species, habitat).

## 2. Methods

### 2.1. Theory: Energy-dependent sigmoid growth models

The generalised sigmoid population growth model with energy dependence that we introduce is:

$$\frac{dN(t)}{dt} = rN(t) f_c(N(t); K, \lambda) \left( f_E(E; \lambda) - f_N(N(t); \lambda) \right), \quad (9)$$

where  $N(t)$  is the population size satisfying  $0 \leq N(t) \leq K$ ,  $r > 0$  is a nominal growth rate,  $E \geq 0$  is the energy available to the population,  $f_c(N(t); K, \lambda) \geq 0$  is a ‘crowding’ function,  $f_E(E; \lambda)$  is an ‘energy dependence’ function,  $f_N(N(t); \lambda) \geq 0$  is a ‘population penalty’ function,  $K > 0$  is a population carrying capacity and  $\lambda$  represents any other constant parameters (where relevant).

The crowding function  $f_c(N(t); K, \lambda) \geq 0$  limits the population’s net growth rate as  $N(t)$  approaches the population carrying capacity  $K$  (Jin et al., 2016; Simpson et al., 2022). The energy dependence function  $f_E(E; \lambda)$  can take positive or negative values and is a monotonically non-decreasing function of  $E$  such that it is zero when the energy is equal to some ‘compensation’ value  $E_c$ , i.e.  $f_E(E_c; \lambda) = 0$ . The population penalty function  $f_N(N(t); \lambda) \geq 0$  limits the population’s efficiency to utilise energy as  $N(t)$  increases and is a monotonically non-decreasing function of  $N(t)$  such that it is zero when the population is zero,  $f_N(0; \lambda) = 0$ . Graphical representations of one potential choice for the functions  $f_N$ ,  $f_c$  and  $f_E$  are shown in Figure 1. Equation (9) is an extension of the general sigmoid growth model (Equation (1)) via inclusion of the additional factor  $(f_E(E; \lambda) - f_N(N(t); \lambda))$  to incorporate energy dependence; this factor is analogous to an Allee effect (Section 1). Note that Equation (9) is only defined for a population  $N$  satisfying  $0 \leq N(t) \leq K$  be-



cause a population cannot be negative, and we wish to avoid non-physical behaviour when  $N(t) > K$  in the case where  $f_c(N(t); K, \lambda) < 0$  and  $(f_E(E; \lambda) - f_N(N(t); \lambda)) < 0$  as such a situation could yield unrestricted growth.

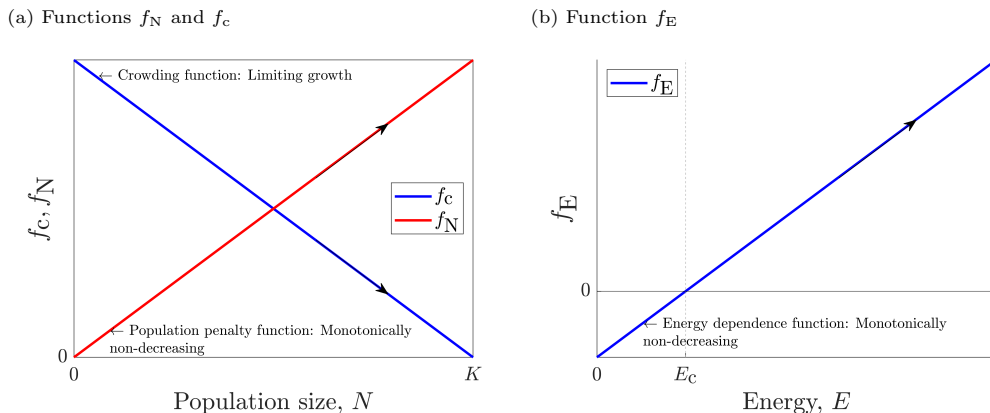


Figure 1: Visual depiction of one potential choice for the functions  $f_N$ ,  $f_c$  and  $f_E$  to be used in the proposed energy-dependent sigmoid growth model, Equation (9). The specific functions  $f_N$ ,  $f_c$  and  $f_E$  depicted here are the linear relationships that form the second model example we introduce, discussed further in Section 2.1.2.

In the following sections, we explain and examine three models adhering to the form of Equation (9) to demonstrate the generality of the introduced model family. In these models we will define  $f_E(E; \lambda)$  and  $f_N(N(t); \lambda)$ , but we will keep the crowding function  $f_c(N(t); K, \lambda)$  general where possible, since forms of  $f_c$  have been readily discussed elsewhere (e.g. Simpson et al. 2022).

Possible steady state values of Equation (9) are  $N^* = 0$ ,  $N^* = K$  or  $N^*$  satisfying  $f_E(E; \lambda) = f_N(N(t); \lambda)$ , for any appropriately chosen crowding function  $f_c(N(t); K, \lambda)$ , such as those listed in Equation (2). Because  $f_E(E; \lambda)$  and  $f_N(N(t); \lambda)$  are both monotonically non-decreasing functions, this implies the inverse function  $f_N^{-1}(f_E(E; \lambda))$  is also a monotonically non-decreasing function, so the steady state  $N^*$  satisfying  $f_E(E; \lambda) = f_N(N(t); \lambda)$  will be a monotonically non-decreasing function of  $E$ . Also note, for logistic and Richards' growth models,  $r$  could be interpreted as an approximation of the per-capita growth rate in the specific case of when both  $N(t)$  is small and  $f_E(E; \lambda) \approx 1$ .

### 2.1.1. Example model 1: Linear energy dependence and no population penalty

The first model adhering to the form of Equation (9) we discuss is hereafter referred to as the ‘Step Model’, described as such due to its steady state behaviour shown in Figure 2. The Step Model has linear energy dependence, where  $f_E(E; \lambda) = (E - E_c)/E_c$ , and no population penalty  $f_N(N(t); \lambda) = 0$ :

$$\frac{dN(t)}{dt} = rN(t)f_c(N(t); K, \lambda) \left( \frac{E - E_c}{E_c} \right), \quad (10)$$

as this yields perhaps the simplest nontrivial form of Equation (9) whereby  $f_E(E; \lambda)$  and  $f_N(N(t); \lambda)$  satisfy the requirements of (1) both functions being monotonically non-decreasing, (2) the energy dependence function being zero at the compensation energy,  $f_E(E; \lambda) = 0$ , and (3) the population penalty function being zero when there is zero population  $f_N(N(t); \lambda) = 0$ . Regardless of whether the crowding function represents logistic, Richards’ or Gompertz growth, Equation (10) has stable steady states of  $N^* = 0$  when  $E < E_c$ , and  $N^* = K$  when  $E > E_c$ . This model therefore only allows the trivial steady states  $N^* = 0$  and  $N^* = K$ , depicted in Figure 2. The model’s behaviour when  $E = E_c$  is of little interest, since in practical biology situations, this precise relationship will be highly unlikely to occur.

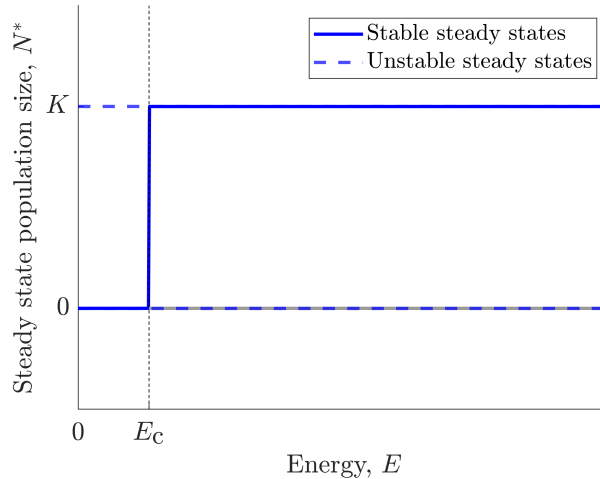


Figure 2: Steady states of the energy-dependent sigmoid growth model with linear energy dependence and no population penalty (Step Model, defined in Equation (10)).

The model defined in Equation (10) and its behaviour is analogous to combining the growth rate  $r$  and energy dependence  $f_E(E; \lambda)$  into an energy-dependent growth rate  $r(E) \leftarrow r \times (E - E_c)/E$ , yielding similarity to time-dependent growth rates (Grozdanski et al., 2009; Irlango et al., 2012; Shepherd et al., 2012; Irlango et al., 2017) and resource- or stressor-dependent growth rates (Baird et al., 2016; Turschwell et al., 2022). However, it is interesting to note that, despite Equation (10) having a linear energy dependence for growth, this does not translate into a linear dependence of the steady states  $N^*$  on energy  $E$  (Figure 2).

### 2.1.2. Example model 2: Linear energy dependence and linear population penalty

The steady state population can become a continuous function of energy if the trivial population penalty function  $f_N(N(t); \lambda)$  chosen in Equation (10) is changed to a slightly less trivial population penalty function  $f_N(N(t); \lambda) = \kappa N(t)$ :

$$\frac{dN(t)}{dt} = rN(t)f_c(N(t); K, \lambda) \left( \frac{E - E_c}{E_c} - \kappa N(t) \right), \quad (11)$$

where  $\kappa > 0$  so that  $f_N(N(t); \lambda)$  is monotonically non-decreasing. This model is hereafter referred to as the ‘Linear Model’, described as such due to its steady state behaviour shown in Figure 3.

Setting  $\kappa = (E_{\text{sat}} - E_c)/(E_c K)$  for convenience, where  $E_{\text{sat}} > E_c$  is a ‘saturation’ value of energy, we find that there are stable steady states  $N^* = 0$  when  $E \leq E_c$ ,  $N^* = K(E - E_c)/(E_{\text{sat}} - E_c)$  when  $E_c \leq E \leq E_{\text{sat}}$ , and  $N^* = K$  when  $E \geq E_{\text{sat}}$  (Figure 3). We caution that this saturation value  $E_{\text{sat}}$  differs from typical ecological interpretations of saturation energy; in the present context,  $E_{\text{sat}}$  refers to the value of energy at which the population reaches the maximum possible value above which no further growth is possible. Thus, the steady state population  $N^*$  depends linearly on energy  $E$  when this energy both exceeds a ‘compensation’ value  $E_c$  and is less than a maximum ‘saturation’ value  $E_{\text{sat}}$ . Equation (11) therefore provides a simple phenomenological model, with easily interpretable parameters, for representing linear energy dependence of steady state populations.

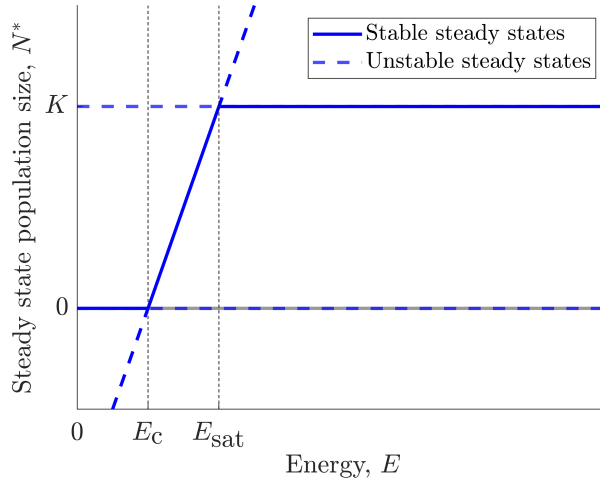


Figure 3: Steady states of the energy-dependent sigmoid growth model with linear energy dependence and linear population penalty (Linear Model, defined in Equation (11)).

### 2.1.3. Example model 3: Logistic growth, linear energy dependence, and nonlinear population penalty derived from geometric arguments for plant cover versus light availability

For the third model examined here, we take a rather different approach to the previous two models; this model is hereafter referred to as the ‘Geometric Model’ due to its derivation discussed later in this section. Both the Step Model and Linear Model (Equations (10) and (11) respectively) are phenomenological in origin, i.e. they are designed intentionally to obtain the desired model characteristics. However, there are multiple ways in which more complicated models could be constructed that adhere to the form of Equation (9). Multiple authors advocate for models that are less phenomenological than the two models described in the previous two sections, and rather desire models based on mechanistic understanding (White and Marshall, 2019). Hence, as a demonstration of the potentially wide application of Equation (9), we here show (surprisingly) that a mechanistic ecological model predicting plant cover responses to light availability derived from geometric arguments (Baird et al., 2016) adheres to the form of Equation (9), when the model’s population dynamics are defined in units of ground area covered by the plant. The application of geometric approaches

to develop models for plant species processes and growth is a well-established practice (Eagleson, 2002) but is less common for population dynamics of other species.

The geometric derivation of this model is advantageous because it expresses dynamics based on a mechanistic understanding; yet it requires only two parameters  $r$  and  $E_c$  whilst also still yielding dependence of steady state populations on energy. Thus, this model retains the benefits of both the Step Model and Linear Model, but also has a mechanistic basis. This model is already being used to represent the dynamics of multiple marine benthic species in a sophisticated environmental modelling suite that is currently being applied to the Great Barrier Reef (Baird et al., 2020).

### Derivation of the Geometric Model

The primary geometric assumption of the Geometric Model is that ‘effective’ ground cover occupied by the population,  $A_{\text{eff}}(t)$ , which is bounded between zero (0% cover) and one (100% cover), increases with population biomass  $B(t)$  proportionally to the unoccupied ground area  $1 - A_{\text{eff}}(t)$  (Baird et al., 2016):

$$\frac{dA_{\text{eff}}(t)}{dB(t)} \propto 1 - A_{\text{eff}}(t). \quad (12)$$

Equation (12) represents the growth of a plant population, where new leaves are randomly placed continuously on the ground area; a fraction  $1 - A_{\text{eff}}(t)$  of these new leaves will cover unoccupied ground area (Baird et al., 2020). Following Baird et al. (2016), we next define the leaf area  $A(t)$  to represent the total area of all leaves, which is a different value to the effective area as viewed from above,  $A_{\text{eff}}(t)$ . Because, when viewed from above, leaves may cover other leaves,  $A(t) \geq A_{\text{eff}}(t)$ , with equality only if no leaf is covering any other leaf. Then, mathematically assuming  $A_{\text{eff}}(t) = 0$  implies  $B(t) = 0$ , and introducing  $\Omega$  as the ratio of plant leaf area to biomass,  $\Omega = A(t)/B(t)$ , one can obtain from Equation (12) that:

$$A_{\text{eff}}(t) = 1 - e^{-\Omega B(t)}, \quad (13)$$

as shown in Appendix B of Baird et al. (2016).

Since Equation (13) considers a plant population, the primary limitation to energy intake (and

subsequent growth) is availability of light for absorption by plant leaves. However, not all plant leaves can absorb light because they may be shaded by other leaves. Thus, for this model it is assumed that the increase  $dB(t)/dt$  in population biomass  $B(t)$  is proportional to the energy absorbed per ground area occupied by the population,  $EA_{\text{eff}}(t)$ , minus the minimum ('compensation') energy needed to fuel the total population biomass,  $E_c A(t) \equiv E_c \Omega B(t)$ :

$$\frac{dB(t)}{dt} \propto [EA_{\text{eff}}(t) - E_c \Omega B(t)]. \quad (14)$$

Writing Equation (14) solely in terms of  $B(t)$ , i.e. without dependence on  $A_{\text{eff}}(t)$ , by substituting Equation (13), yields:

$$\frac{dB(t)}{dt} \propto \left[ E \left( 1 - e^{-\Omega B(t)} \right) - E_c \Omega B(t) \right]. \quad (15)$$

Equation (15) is the foundation of sophisticated models of seagrass, corals and macroalgae used in Baird et al. (2016, 2020), although see Appendix B.1 of Adams et al. (2018) for a partial deconstruction of these complicated models towards a form analogous to Equation (15). These previous works considered plant population in units of biomass (Baird et al., 2016, 2020) or leaf area index (Adams et al., 2018). In the present work, we rewrite Equation (15) in units of plant-occupied ground cover via application of the chain rule:

$$\frac{dA_{\text{eff}}(t)}{dt} = \frac{dA_{\text{eff}}(t)}{dB(t)} \frac{dB(t)}{dt}. \quad (16)$$

Setting  $r/E_c$  as the constant of proportionality in Equation (15), and combining the resulting equation with Equations (13) and (16), yields:

$$\frac{dA_{\text{eff}}(t)}{dt} = rA_{\text{eff}}(t)(1 - A_{\text{eff}}(t)) \left[ \frac{E - E_c}{E_c} - \frac{\ln((1 - A_{\text{eff}}(t))^{-1}) - A_{\text{eff}}(t)}{A_{\text{eff}}(t)} \right]. \quad (17)$$

Comparing Equations (9) and (17), we see that the derived Geometric Model (Equation (17)) is

a particular case of the energy-dependent sigmoid growth model introduced in Equation (9), where:

$$N(t) = A_{\text{eff}} \quad (18)$$

$$K = 1 \quad (19)$$

$$f_c(N(t); K, \lambda) = 1 - \frac{N(t)}{K} \quad (20)$$

$$f_E(E; \lambda) = \frac{E - E_c}{E_c} \quad (21)$$

$$f_N(N(t); \lambda) = \frac{K \ln((1 - N(t)/K)^{-1}) - N(t)}{N(t)}. \quad (22)$$

Thus, we rewrite here the Geometric Model, for consistency with the other models, in the more general form:

$$\frac{dN(t)}{dt} = rN(t) \left(1 - \frac{N(t)}{K}\right) \left[ \frac{E - E_c}{E_c} - \frac{K \ln((1 - N(t)/K)^{-1}) - N(t)}{N(t)} \right]. \quad (23)$$

The crowding function  $f_N(N(t); \lambda)$  of the Geometric Model is logistic growth (Equation (2a)), and the energy dependence function  $f_E(E; \lambda)$  of the Geometric Model is the same as the Step Model and Linear Model, which already satisfies the required properties of being a monotonically non-decreasing function of  $E$  and  $f_E(E_c; \lambda) = 0$ . The population penalty function  $f_N(N(t); \lambda)$  of the Geometric Model seems unwieldy, but it does not require definition of additional parameters  $\lambda$  and is in fact a monotonically non-decreasing function of  $N(t)$  between  $0 \leq N(t) \leq K$ . Also note that  $\lim_{N \rightarrow 0^+} f_N(N(t); \lambda) = 0$  and  $\lim_{N \rightarrow K} f_N(N(t); \lambda) \rightarrow +\infty$ , and this latter limit does not cause the Geometric Model to be undefined at  $N(t) = K$  since overall  $\lim_{N \rightarrow K} dN(t)/dt = 0$  due to the crowding function. Finally, Equation (23) implies that  $r$  can be physically interpreted as the per-capita growth rate when  $N(t)$  is small and  $E = 2E_c$ , i.e. when the population is receiving double its minimum requirements of energy.

### Steady states of the Geometric Model

The steady state populations for the Geometric Model, which are the equilibria of Equation

(23), satisfy:

$$0 = rN^* \left(1 - \frac{N^*}{K}\right) \left[ \frac{E - E_c}{E_c} - \frac{K \ln((1 - N^*/K)^{-1}) - N^*}{N^*} \right], \quad (24)$$

for which it is clear that  $N^* = 0$ ,  $N^* = K$ , and there is a third steady state  $N^*$  that satisfies the equation:

$$\frac{E - E_c}{E_c} = \frac{K \ln((1 - N^*/K)^{-1}) - N^*}{N^*}. \quad (25)$$

Equation (25) has the solution:

$$N^* = \frac{K}{E} \left( E_c W \left( -\frac{E \exp(-E/E_c)}{E_c} \right) + E \right), \quad (26)$$

where  $W(\cdot)$  is the principal branch of Lambert W function (Corless et al., 1996); the Lambert W function  $W(x)$  outputs solutions  $w$  of the equation  $we^w = x$ .

The steady state  $N^* = 0$  is stable for  $E < E_c$  and the steady state represented by Equation (26) is stable for  $E > E_c$ . The steady state  $N^* = K$  is unstable. These steady states are depicted in Figure 4. A summary of the stable steady states for Models 1 to 3 is provided in Table 1.

Table 1: Summary of stable steady states for the energy-dependent sigmoid growth models defined here as Models 1 to 3 (Equations (10), (11) and (23), respectively). For a graphical description of the stable and unstable steady states, see Figures 2, 3 and 4.  $W(\cdot)$  is the principal branch of the Lambert W function (Corless et al., 1996).

Value of energy $E$	Step Model	Linear Model	Geometric Model
$E < E_c$	0	0	0
$E_c < E < E_{\text{sat}}$	$K$	$K(E - E_c)/(E_{\text{sat}} - E_c)$	$(K/E)(E_c W(-E \exp(-E/E_c)/E_c) + E)$
$E > E_{\text{sat}}$	$K$	$K$	$(K/E)(E_c W(-E \exp(-E/E_c)/E_c) + E)$



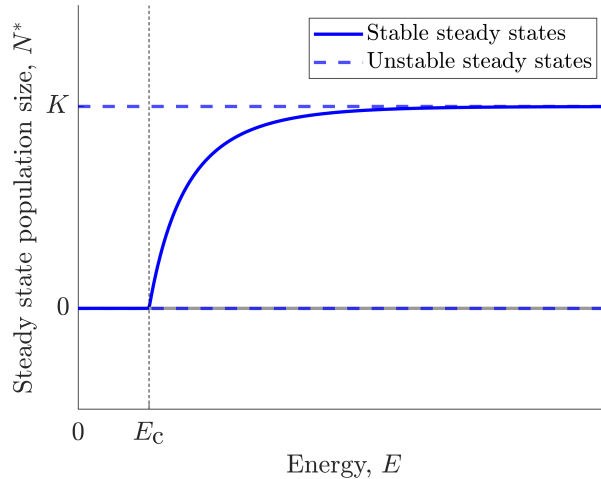


Figure 4: Steady states of the energy-dependent sigmoid growth model with logistic growth, linear energy dependence and nonlinear population penalty, derived from geometric arguments for plant cover vs light availability (Geometric Model, defined in Equation (23)).

Advantageously, the Geometric Model only has three parameters to be estimated ( $r$ ,  $K$  and  $E_c$ ), as it is a model based primarily on geometric arguments, and so allows for nuanced effects from environmental conditions in the form of energy or light received,  $E$ . For example, received light is a critical value for determining the composition of shallow water communities (Miller and Etter, 2008), and in particular the growth of macroalgae (Dummermuth and Wiencke, 2003). In the next section, we compare all three models described thus far for their ability to fit observed data for macroalgae populations constrained by light availability in shallow waters adjacent to Antarctica.

## 2.2. Application to Antarctic benthic algae

### 2.2.1. Data sources and interpretation

Datasets were obtained by Clark et al. (2013a) for several Antarctic shallow-water sites around Casey Station, located in the Windmill Islands, on the coast of Wilkes Land, East Antarctica (Figure 5). Of these sites, we used data from McGrady Cove (MC), Newcomb Corner (NC), O'Brien Bay 1 (OB1), O'Brien Bay 3 (OB3), O'Brien Bay 5 (OB5), Shannon Bay (SB) and Shirley Island (SI). The location of these sites are depicted in Figure 5. This data includes dates of sea-ice

break-out and daily light measurements from each of the aforementioned sites (Clark et al., 2013b).

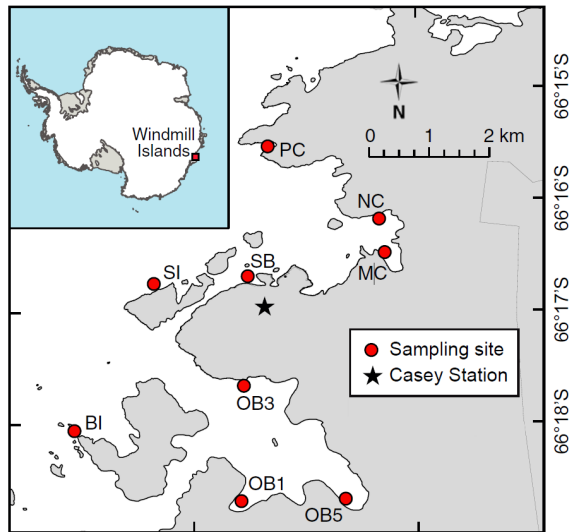


Figure 5: Map of study area where data used in the present study was collected. Inset shows the location of the Windmill Islands, on the coast of Wilkes Land, East Antarctica; all sampling sites were at this location. PC = Powell Cove, NC = Newcomb Corner, MC = McGrady Cove, SB = Shannon Bay, SI = Shirley Island, OB1 = O'Brien Bay 1, OB3 = O'Brien Bay 3, OB5 = O'Brien Bay 5 and BI = Beall Island. Sites PC and BI were excluded from the present study as there is no light data available for these sites. Figure adapted from Clark et al. (2013a).

Light measurements were obtained at each of the aforementioned sites using light sensors positioned at depths of 7–10 metres (Clark et al., 2013a). Measurements from the Shirley Island site (SI) were used by Clark et al. (2013a) to approximate the expected daily light reaching the sea-bed in the absence of sea-ice for one year: as sea-ice is only present at SI for approximately 3 months during winter when there is little daily light (Clark et al., 2013a), SI is the site that most closely resembles conditions in the absence of sea-ice year-round. Clark et al. (2013a) achieved this by fitting a periodic function to the light data from the SI site to obtain modelled daily light dose; a comparison between this modelled daily light dose and the measured daily light values is shown in Figure 6. The modelled daily light values (blue line in Figure 6) form the basis of our estimation of the expected light dose for different dates of sea-ice break-out (discussed in detail in Section 2.2.2).

In this work we consider the *daily* light dose, rather than *instantaneous* light values, so all light measurements are stated in units of  $\text{mol m}^{-2} \text{d}^{-1}$  to allow direct comparison between the data collected by Clark et al. (2013a) and the outputs of our models (discussed further in Section 3). All

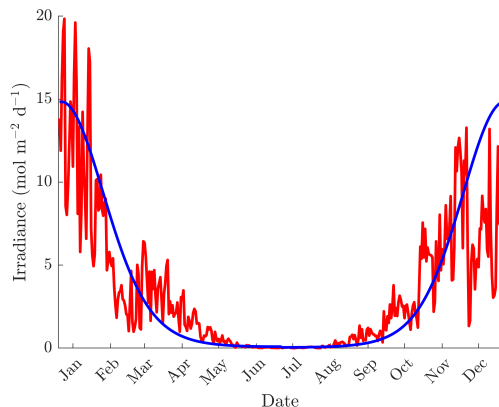


Figure 6: Comparison between the measured daily light dose (red) at the Shirley Island site (SI) and the daily modelled light dose as a periodic function of the date by Clark et al. (2013a) (blue).

light values used here refer to the solar radiation available for photosynthesis, commonly referred to as photosynthetically active radiation (PAR).

The data obtained by Clark et al. (2013a) also includes multiple measurements of algae cover and invertebrate cover for each site, with measurements being taken at depths of 6 m and 12 m from both top-oriented and side-oriented surfaces of boulders. There are inherent differences in the amount of light available to algae on each of these boulder surface orientations, due to processes such as self-shading (Baird et al., 2016, 2020), sedimentation (Knott et al., 2004; Clark et al., 2017) and light attenuation (Mitchell et al., 1991) affecting these surfaces differently.

Invertebrate cover measurements were reported by Clark et al. (2013a) in two ways: cover occupied by all invertebrates, and cover occupied by all invertebrates excluding the two most abundant invertebrate species, *Inversiula nutrix* and *Spirorbis nordenskjoldi*, that were universally dominant at all sites. We will refer to these two measurement types as ‘abundant invertebrates’ and ‘nonabundant invertebrates’, respectively.

Two algae species, *Desmarestia menziesii* and *Himantothallus grandifolius*, form algal canopies at the site SI. These canopies form at locations that have high light availability, and were therefore not observed at the other sites (Clark, pers. comm.). Clark et al. (2013a) obtained data at the SI site from underneath both of these canopies, although we note the canopies themselves did not

form part of the algae cover measurements. In the present work, in order to compare algae cover between sites, for SI we only used data taken from underneath canopies formed by *Desmarestia menziesii*; this canopy is more diffuse and lets more light through than *Himantothallus grandifolius*, and therefore more closely resembles the conditions of canopy absence (Clark, pers. comm.).

There are three biological interpretations of the algae cover data in terms of the maximum cover that the algae can possibly occupy, which we will hereafter refer to as three different ‘interpretations’ for ease of reference. Firstly, we can treat the algae cover measurements as absolute values, in which case we interpret that there is some non-biological and constant process responsible for preventing the maximum cover from reaching 100% (e.g. sedimentation, which may affect measurements from the tops and sides of boulders differently) and therefore the carrying capacity  $K < 100\%$ . Secondly, we can consider the ratio of algae cover to the cumulative cover of algae and invertebrates, where we interpret any space not occupied by algae or invertebrates as being uninhabitable, with non-biological processes affecting each site differently, and therefore the carrying capacity  $K = 100\%$ . Finally, we can consider the ratio of algae cover to the cumulative cover of algae and nonabundant invertebrates, and so interpret that any space not occupied by algae or nonabundant invertebrates is uninhabitable, with the abundant invertebrate species and non-biological processes both limiting space and affecting each site differently, and therefore the carrying capacity  $K = 100\%$ .

Data for the two boulder orientations (top and side) can be interpreted in any of the three options described above, resulting in what we refer to as six ‘scenarios’. Table 2 summarises the algae cover data measured by Clark et al. (2013a) for each scenario. We chose to aggregate the measurements taken at 6 m and 12 m depths to use in the present work, for three reasons. Firstly, although we expected a decrease in measured algae cover as the depth increased from 6 m to 12 m, this was only the case at two sites; one site consistently measured zero, while at the remaining four sites, for both top- and side-oriented surfaces, there was a clear *increase* in measured algae cover as the depth increased from 6 m to 12 m. Secondly, we are operating under the assumption that the presence of sea-ice eliminates light completely, and that the presence or absence of sea-ice has a greater influence on light availability than the difference in depths. Finally, the light data was obtained at depths of 7–10 m, which is not precisely representative of the depths of the

algae measurements. The choice of aggregating the algae measurements at both depths will yield predicted measurements that most closely match with the light data available for the present study.

Table 2: Percentage of algae cover found at each site by Clark et al. (2013a) (mean  $\pm$  standard deviation, obtained from 16 replicate measurements) for each scenario (combination of boulder orientation and data interpretation). Sites are listed in order of decreasing annual light dose for each boulder surface orientation. Predicted annual light refers to an annual light dose calculated by combining a modelled curve fitted to Shirley Island’s data (blue line in Figure 6) together with an assumed date of sea-ice break-out for each site (see Section 2.2.2 for full details). See Figure 5 caption for site abbreviations.

Boulder surface orientation	Site	Algae cover relative to all invertebrates (%)	Algae cover relative to nonabundant invertebrates (%)	Absolute algae cover (%)	Measured annual mean light (mol m <sup>-2</sup> d <sup>-1</sup> )	Predicted annual mean light (mol m <sup>-2</sup> d <sup>-1</sup> )
Side	SI	41.0 $\pm$ 28.4	78.4 $\pm$ 28.4	31.9 $\pm$ 25.0	3.74	3.42
	OB3	60.1 $\pm$ 19.7	90.1 $\pm$ 10.6	15.1 $\pm$ 13.6	1.95	1.53
	NC	23.7 $\pm$ 30.6	42.9 $\pm$ 36.3	6.7 $\pm$ 10.3	1.36	1.06
	SB	19.5 $\pm$ 21.1	54.3 $\pm$ 30.3	6.4 $\pm$ 7.9	0.78	1.31
	MC	10.8 $\pm$ 12.9	25.1 $\pm$ 27.2	4.0 $\pm$ 5.3	0.62	0.30
	OB5	17.8 $\pm$ 24.8	30.1 $\pm$ 28.6	8.1 $\pm$ 13.4	0.14	0.18
	OB1	0 $\pm$ 0	0 $\pm$ 0	0 $\pm$ 0	0.14	0.15
Top	SI	48.3 $\pm$ 37.5	55.8 $\pm$ 37.2	46.1 $\pm$ 36.9	3.74	3.42
	OB3	91.2 $\pm$ 7.0	91.7 $\pm$ 7.1	46.0 $\pm$ 19.1	1.95	1.53
	NC	40.1 $\pm$ 34.9	52.0 $\pm$ 27.7	20.0 $\pm$ 21.5	1.36	1.06
	SB	75.3 $\pm$ 24.3	77.7 $\pm$ 20.6	36.2 $\pm$ 32.2	0.78	1.31
	MC	35.8 $\pm$ 23.6	42.2 $\pm$ 25.3	16.9 $\pm$ 18.8	0.62	0.30
	OB5	52.0 $\pm$ 37.8	66.9 $\pm$ 37.5	44.4 $\pm$ 36.4	0.14	0.18
	OB1	0 $\pm$ 0	0 $\pm$ 0	0 $\pm$ 0	0.14	0.15

## 2.2.2. Ranges of light values

In this work, we assumed that sea-ice reformation occurs on 1 April (as also assumed in Clark et al. (2013a)) and therefore approximated the annual light dose for sea-ice break-out dates ranging from 2 April (1 day of ice cover) to 31 March the following year (365 days of ice cover). This was achieved using the modelled light function (blue line in Figure 6); we replaced the benthic light values modelled by Clark et al. (2013a) with  $E = 0$  mol m<sup>-2</sup> day<sup>-1</sup> for days where sea-ice cover was assumed to be in place at each site (see Supplementary Material Appendix S1 to see how the measured and modelled curves compare) then obtaining the annual light dose by averaging over one year. This mathematical process assumes that the benthic light experienced by algae in the absence of ice cover follows the modelled curve shown in Figure 6.

Figure 7 shows the outcome of this mathematical process: the modelled annual light dose for each date of sea-ice break-out (blue line), as well as the measured (black circles) and modelled (red crosses) annual light dose at each of the seven sites. This light series is used in subsequent

computations to estimate the timing of the tipping point between the benthic ecosystem being dominated by invertebrates or algae (discussed further in Section 2.2.6).

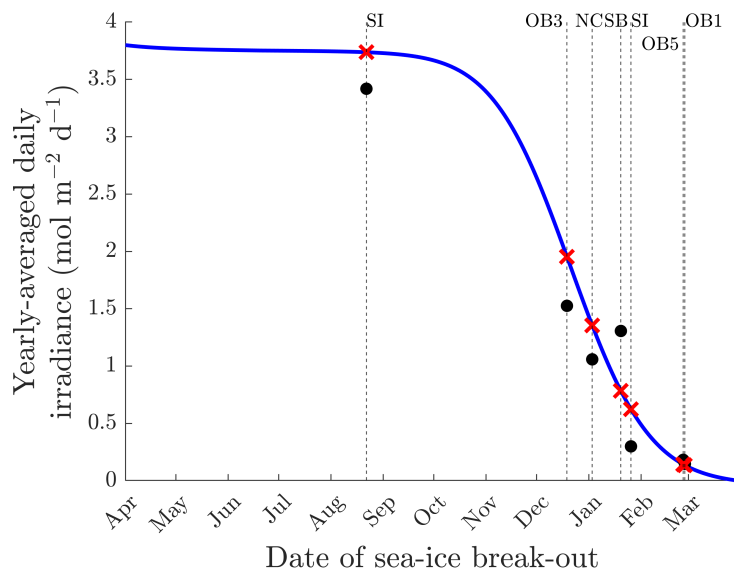


Figure 7: Modelled (blue) annual light dose, represented as daily light values averaged over one year, obtained by replacing benthic light values modelled by Clark et al. (2013a) with  $E = 0 \text{ mol m}^{-2} \text{ d}^{-1}$  on days where the benthic communities are assumed to experience complete darkness due to sea-ice cover prior to the date of sea-ice break-out. Also shown is the measured annual light dose at each site (black) and the corresponding modelled annual light dose (red crosses). This figure assumes that sea-ice reforms on 1 April and the benthic light follows the modelled curve shown in Figure 6. See Figure 5 for site abbreviations.

### 2.2.3. Biological assumptions when fitting models to the data

In the present analysis, we assumed that the algae populations have reached a steady state and are thus representative of habitat suitability. We recognise that this assumption, albeit implicitly made also in Clark et al. (2013a), is not guaranteed to hold (Hastings et al., 2018), but is practical given the available data. We consider the three models discussed in Sections 2.1.1 to 2.1.3 for their ability to fit the data from Clark et al. (2013a). In all three models, the growth rate parameter  $r$  does not affect the steady state and therefore the data cannot be used to estimate this parameter, since we assume that algae populations have stabilised in time. However, if there are estimates of  $r$  (such as in Wiencke 1990a,b; Gómez and Wiencke 1997), one could feasibility use these estimates

together with the available data to parameterise the dynamic versions of the three models, if the desired application was to predict temporal changes in algae cover.

#### 2.2.4. Bayesian inference for fitting models to the data

The steady states of the three models detailed in Sections 2.1.1 to 2.1.3 (summarised in Table 1) were calibrated to each of the six ‘scenarios’ (see Section 2.2.1) using Bayesian inference. Bayesian inference is a robust statistical framework that can be used for estimation and quantification of the uncertainty in model parameters (Girolami, 2008). Bayesian inference was implemented in this work using Sequential Monte Carlo (SMC) sampling due to its ability to exploit parallel computing architecture (Dai et al., 2022).

Bayesian inference was used to estimate joint posterior distributions for between 2 and 4 parameters (depending on the scenario): the compensation irradiance  $E_c$  ( $\text{mol m}^{-2} \text{ d}^{-1}$ ), saturation irradiance  $E_{\text{sat}}$  ( $\text{mol m}^{-2} \text{ d}^{-1}$ ; estimated for the Linear Model only), carrying capacity  $K$  (% cover; estimated for two of the three data interpretations, see Section 2.2.1), and the standard deviation  $\sigma$  characterising the model-data fit (in units of % cover). A Gaussian likelihood function (characterised by the aforementioned standard deviation  $\sigma$ ) was assumed. A joint prior distribution was chosen to enforce physical requirements of the system, whilst simultaneously being as uninformative as possible (Banner et al., 2020). With the exception of the Linear Model (discussed in the next paragraph), the joint prior distribution was simply the product of independent uniform prior distributions for each parameter.

Although all models required estimation of the compensation irradiance  $E_c$ , the Linear Model was the only model we investigated that also required estimation of the saturation irradiance  $E_{\text{sat}}$ ; since it is a physical requirement that  $E_{\text{sat}} > E_c$  we enforced this in the prior distribution for model-data calibrations involving the Linear Model. This means that the joint prior distribution for the Linear Model parameters was only nonzero if  $E_{\text{sat}} > E_c$ , thus making the prior distribution for these two parameters non-independent in the Linear Model.

The lower and upper bounds of the prior uniform distributions for individual parameters were chosen as follows. For the standard deviation  $\sigma$  and carrying capacity  $K$  (where applicable), we

chose prior bounds of  $[0, 100\%]$ , representing the entire range of possible values for these parameters. For the compensation irradiance  $E_c$ , we chose prior bounds of  $[0, 5 \text{ mol m}^{-2} \text{ d}^{-1}]$ , because the minimum light requirements of algae should exceed zero light, and the chosen maximum bound for  $E_c$  is greater than both the measured and modelled maximum annual light dose experienced by any site in our available data. For the saturation irradiance  $E_{\text{sat}}$  we chose prior bounds of  $[0, 15 \text{ mol m}^{-2} \text{ d}^{-1}]$ , to ensure a sufficiently (but not excessively) wide range of possible values for this parameter.

The SMC algorithm we implemented in this work was adapted from Adams et al. (2020a,b), with an additional resampling step included as described in Vilas et al. (2021) to ensure equal weighting of posterior samples. We report the estimated value for each parameter as the mean  $\pm$  standard deviation of the posterior samples (obtained from 1000 samples). Each calibrated model was then used to forecast algae cover over a range of annual light doses (discussed further in Sections 2.2.5 and 2.2.6). Forecasts included 68% and 95% central credible intervals to represent uncertainty, calculated using the posterior predictive distributions obtained from the SMC sampling.

### 2.2.5. Model selection and prediction methods

When fitting each of the three models to the data of Clark et al. (2013a), the model with the lowest estimated value of the model-data fit discrepancy  $\sigma$  was treated as the ‘best’ model. We report these values of  $\sigma$  in units of % cover, and it is therefore an absolute rather than relative measure. This measure of goodness of fit is applicable only when model complexity is disregarded, and we recognise that formal model selection procedures could also be used to penalise model complexity if desired (Johnson and Omland, 2004; Tredennick et al., 2021; Warne et al., 2019).

### 2.2.6. Prediction of tipping points

The calibrated models were used to forecast algae cover over a range of annual light doses and the corresponding range of sea-ice break-out timing dates (discussed in Section 2.2.2). These forecasts were used to estimate the date of sea-ice break-out at which a shift in the *timing* of this date would yield the greatest change in steady state algae cover, as a coarse estimate for the timing of a tipping



point in algae cover. We also calculated the predicted rate of change in algae cover with respect to the date of sea-ice break-out associated with each estimated tipping point. We report estimations of the greatest change in algae cover only for the Geometric Model as the mean  $\pm$  standard deviation calculated from the posterior samples. In the case of the Step Model, the maximum rate of change is mathematically infinite at the location of the switch in steady states (see e.g. Figure 2), while in the case of the Linear Model, the tipping point predictions are a result of mathematical artefacts due to its functional form (for further information, refer to Supplementary Material Appendix S2).

### 3. Results

#### 3.1. Fitting the models to the data

All three tested models (described in Sections 2.1.1 to 2.1.3) were fitted successfully to the six different datasets of algae cover versus annual light dose (termed ‘scenarios’, see Section 2.2.1), using Bayesian inference implemented via SMC sampling (Table 3).

Figure 8 shows the model-data fits for one of the six ‘scenarios’: data taken from the sides of boulders, interpreted as relative to the cumulative cover of algae and nonabundant invertebrates. Figures 8a, 8c and 8e show how the models fit to the data for this particular scenario for a range of annual light doses, from 0 to 10 mol m<sup>-2</sup> d<sup>-1</sup>. These figures show how the predicted algae cover is 0% when the annual light dose  $E < E_c$ , and the algae cover increases towards the carrying capacity  $K$  once the annual light dose exceeds  $E_c$ . Note that the plotted credible intervals represent uncertainty in the best-fit model rather than uncertainty in model predictions of new observations, so the plotted credible intervals will necessarily be narrower than the data used to inform them. Figures 8b, 8d and 8f show the algae cover model-data fits now plotted against the date of sea-ice break-out (for sea-ice cover ranging in duration from 1 to 365 days) instead of annual light dose. We note that there is a nonlinear relationship between the quantities of date of sea-ice break-out and annual light dose (Clark et al., 2013a), and this is highlighted particularly when comparing Figures 8c and 8d (the same algae cover model-data fits plotted against these two quantities).

Table 3: Predicted values for all model parameters, including the compensation irradiance  $E_c$ , saturation irradiance  $E_{\text{sat}}$ , standard deviation  $\sigma$  and maximum possible algae cover (carrying capacity  $K$ ) (mean  $\pm$  standard deviation, obtained from 1000 simulations) for calibrated models. Details of the models are provided in Sections 2.1.1 to 2.1.3, and explanations of the data interpretations are provided in Section 2.2.1.

Scenario	Model	$E_c$ (mol m <sup>-2</sup> day <sup>-1</sup> )	$E_{\text{sat}}$ (mol m <sup>-2</sup> day <sup>-1</sup> )	$\sigma$ (%)	$K$ (%)
Top data, relative to all	Step	1.18 $\pm$ 0.08	-	45.1 $\pm$ 3.1	-
	Linear	0.04 $\pm$ 0.07	1.79 $\pm$ 0.14	38.9 $\pm$ 2.7	-
	Geometric	0.77 $\pm$ 0.06	-	41.4 $\pm$ 2.7	-
Top data, relative to nonabundant	Step	0.17 $\pm$ 0.08	-	44.4 $\pm$ 3.0	-
	Linear	0.02 $\pm$ 0.02	1.64 $\pm$ 0.19	39.2 $\pm$ 2.7	-
	Geometric	0.17 $\pm$ 0.13	-	41.4 $\pm$ 3.0	-
Top data, absolute	Step	0.17 $\pm$ 0.01	-	28.4 $\pm$ 2.1	35 $\pm$ 3
	Linear	0.14 $\pm$ 0.04	0.22 $\pm$ 0.22	28.7 $\pm$ 2.0	35 $\pm$ 3
	Geometric	0.12 $\pm$ 0.04	-	29.8 $\pm$ 2.1	36 $\pm$ 3
Side data, relative to all	Step	3.31 $\pm$ 1.36	-	37.9 $\pm$ 2.4	-
	Linear	0.06 $\pm$ 0.06	6.02 $\pm$ 0.60	27.1 $\pm$ 1.9	-
	Geometric	1.13 $\pm$ 0.10	-	32.6 $\pm$ 2.1	-
Side data, relative to nonabundant	Step	1.18 $\pm$ 0.08	-	39.2 $\pm$ 2.7	-
	Linear	0.05 $\pm$ 0.09	1.97 $\pm$ 0.13	29.8 $\pm$ 2.1	-
	Geometric	0.82 $\pm$ 0.04	-	31.4 $\pm$ 2.1	-
Side data, absolute	Step	1.77 $\pm$ 0.58	-	14.7 $\pm$ 1.1	27 $\pm$ 5
	Linear	0.33 $\pm$ 0.26	7.24 $\pm$ 2.33	13.4 $\pm$ 1.0	69 $\pm$ 20
	Geometric	1.14 $\pm$ 0.09	-	13.6 $\pm$ 1.0	33 $\pm$ 4

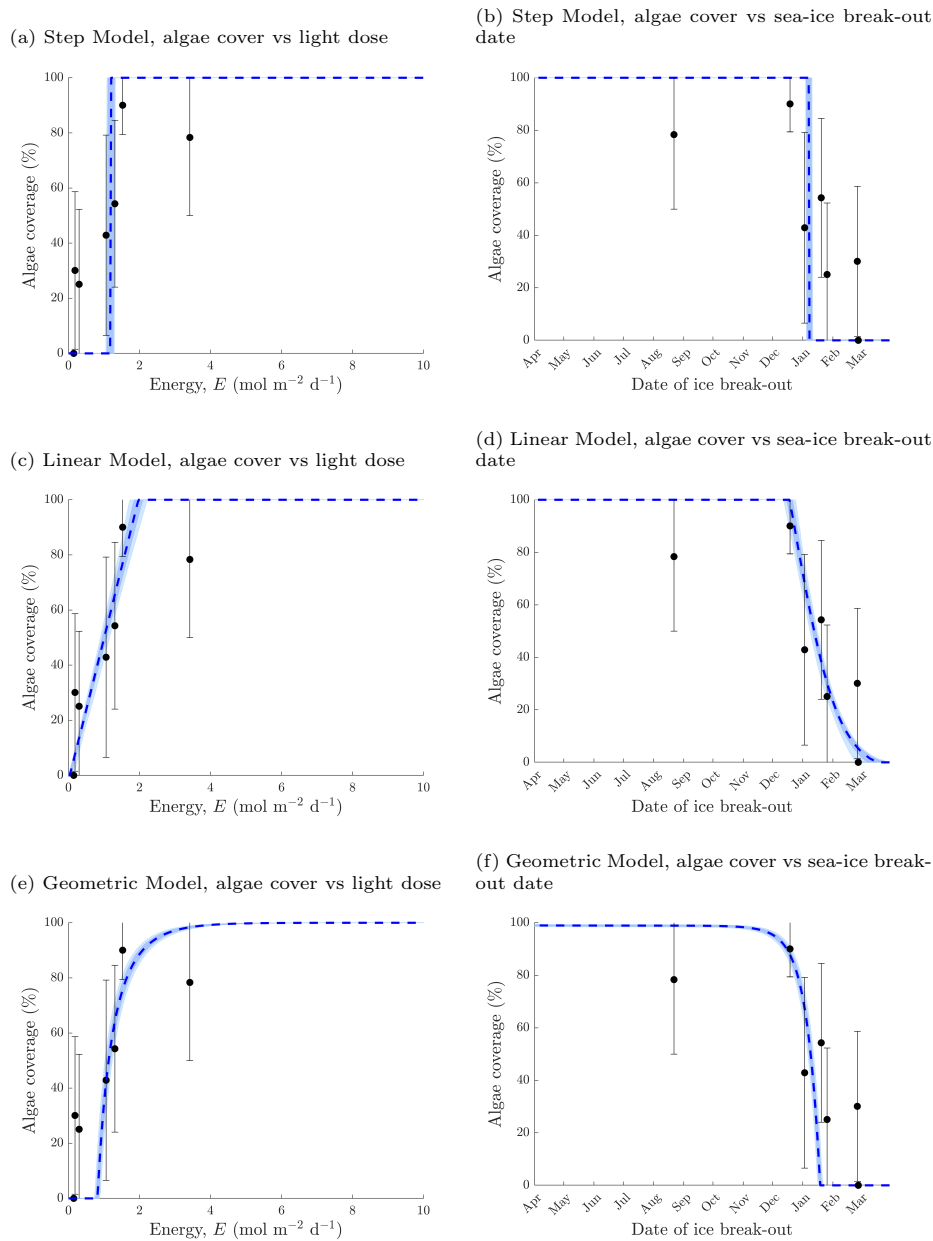


Figure 8: Model-data fits for side-oriented surfaces of boulders, interpreting the data as relative to the cumulative cover of nonabundant invertebrates and algae. Algae cover forecasts for a range of values of annual light dose  $E$  (in units of  $\text{mol m}^{-2} \text{d}^{-1}$ ) are shown for the (a) Step Model, (c) Linear Model and (e) Geometric Model (see Sections 2.1.1 to 2.1.3 for model details). Plotting these forecasts against a range of dates of ice break-out for the (b) Step Model, (d) Linear Model and (f) Geometric Model demonstrate the nonlinear relationship between annual light dose and date of sea-ice break-out. Median model predictions are shown by the dashed lines, the 68% credible intervals are shown by the dark blue shaded regions, and the 95% credible intervals are shown by the light blue shaded regions. Note that these credible intervals represent uncertainty in best-fit models rather than uncertainty in model predictions of new observations, so the plotted credible intervals will necessarily be narrower than the data used to inform them. The forecasts are compared to the data obtained by Clark et al. (2013a) at seven sites (Table 2). (Refer to Supplementary Material Appendix S3 for the model-data fits of the remaining five scenarios.)

We next discuss, in the following sections, how our results show differences between the performance of each model in terms of fitting to each set of data (Section 3.2), differences between datasets in the estimated parameter values (Section 3.3), and differences between datasets in both the predicted timing of tipping points and the rate at which algae cover increases at those tipping points (Section 3.4).

### 3.2. Model fit comparison

The Linear Model was generally the best-fitting model (Table 3, Figure 9), because it had the lowest value of  $\sigma$  (see Section 2.2.5 for justification of this metric) in five out of the six scenarios, followed by the Geometric Model. The Step Model generally had the highest values of  $\sigma$ . However, it is worth noting that the Linear Model has one additional free parameter ( $E_{\text{sat}}$ ) that the other two models do not possess, which likely impacted this finding. Furthermore, the differences in  $\sigma$  between datasets is larger than the differences in  $\sigma$  between models, and there is a distinct improvement in model-data fit (reduced  $\sigma$ ) from top- to side-oriented surfaces (Table 3, Figure 9).

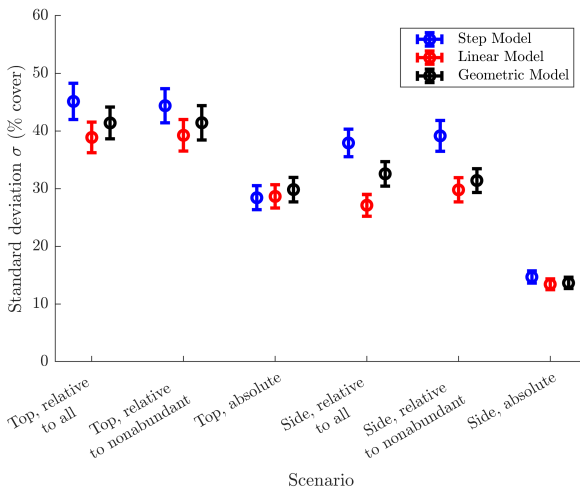


Figure 9: Estimates of the standard deviation  $\sigma$  (mean  $\pm$  error) which characterises the goodness-of-fit for all scenarios for each model. It is clearly seen that the estimates for the scenarios involving the side-oriented surfaces of boulders are lower than the scenarios involving the corresponding top-oriented surfaces, for all models.

### 3.3. Parameter estimations

The vast majority of parameters estimated were well constrained by the data (see Supplementary Material Appendix S4 to see the marginal posterior distributions for all parameters). Thus, most parameters were practically identifiable (Browning et al., 2020), indicating the complexity of the model matched well with the available data in this study.

The compensation irradiance  $E_c$  is an important parameter to estimate because it indicates the minimum annual light dose below which the habitat is unsuitable for long-term algae survival. Estimates of  $E_c$  were highly variable, spanning two orders of magnitude from  $\approx 0.02$  to  $\approx 3$  mol m<sup>-2</sup> d<sup>-1</sup> (Table 3).

Interestingly, we found that for each model, the estimates for  $E_c$  were always lower for the top-oriented surfaces, compared to the corresponding data taken from the side-oriented surfaces (Figure 10). It therefore follows that algae located on side-oriented surfaces require more light in order to achieve the same growth as algae located on top-oriented surfaces. This is physically reasonable because, for example, the effective area for algae to absorb light on side-oriented surfaces will be less than top-oriented surfaces as the former experience a greater impact from self-shading.

For completeness, we acknowledge here that two of the 18 estimates of  $E_c$ , which are from the Step Model for the sides of boulders have high uncertainty (standard deviation  $> 0.5$  mol m<sup>-1</sup> d<sup>-1</sup>, obtained from data interpreted as ‘relative to all’ and ‘absolute’, see Table 3). These uncertain estimates appear to be due to the limited number of sites at which sides of boulders were subjected to high annual light doses ( $\gtrsim 2$  mol m<sup>-2</sup> d<sup>-1</sup>, see Figures S3.1 and S3.2).

The saturation irradiance  $E_{\text{sat}}$ , which indicates the maximum annual light dose above which the long-term algae cover cannot be further increased by receiving additional light, could be estimated from fitting the Linear Model to the data. These estimates of  $E_{\text{sat}}$ , like the estimates of  $E_c$ , were highly variable, ranging from  $\approx 0.2$  to  $\approx 7$  mol m<sup>-2</sup> d<sup>-1</sup> (Table 3). Also similarly to  $E_c$ , estimates of  $E_{\text{sat}}$  were always lower for the top-oriented surfaces, compared to data taken from the side-oriented surfaces. This provides further support for our (physically reasonable) assertion that algae located on side-oriented surfaces require more light than algae on top-oriented surfaces in order to

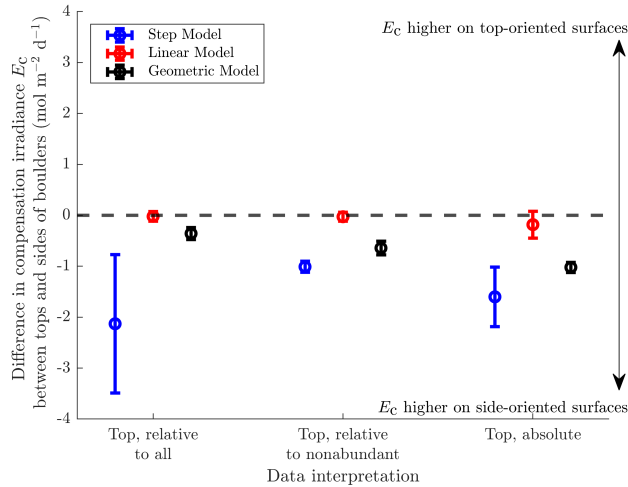


Figure 10: Difference between the model-predicted estimates of the compensation irradiance  $E_c$  between tops and sides of boulders for each relevant combination of data interpretation and model. Details of the models are provided in Sections 2.1.1 to 2.1.3, and explanations of the data interpretations are provided in Section 2.2.1. Positive values indicate the value of  $E_c$  is higher for top-oriented surfaces, while negative values indicate  $E_c$  is higher for side-oriented surfaces. Error bars were calculated using standard error propagation formulae from the mean and standard deviations listed in Table 3.

maximise their growth. However, it should be noted that two of the six estimates of  $E_{\text{sat}}$  exceeded the maximum measured annual light dose; additional data is therefore likely needed to provide a more definitive upper bound on the true value of  $E_{\text{sat}}$ .

The maximum possible algae cover (carrying capacity  $K$ ) was also predicted, for scenarios where the algae cover data was interpreted as absolute values. This maximum algae cover was predicted to be approximately 25-35% for five out of the six combinations of the three models (Step, Linear and Geometric) and two surface orientations (tops and sides of boulders). The sixth, outlier, prediction of carrying capacity  $K$  was made using the Linear Model, which requires more data than the other two models to estimate  $K$  due to its additional free parameter  $E_{\text{sat}}$ , on a dataset which is less informative about carrying capacity (Figure S3.1) than the other ('absolute') dataset tested (Figure S3.3).

Unlike the values predicted for  $E_c$  and  $E_{\text{sat}}$ , where the magnitude of the predicted values were dependent on the boulder surface orientation, the values predicted for  $K$  were more consistent, with no obvious difference between boulder surface orientations. We therefore hypothesise that 25-35%

cover could represent an upper limit to how much space may be occupied by benthic algae in the shallow waters around Antarctica.

### 3.4. Tipping point predictions

Possible tipping points were identified from the annual light dose, and corresponding sea-ice break-out date, that yielded the greatest predicted rate of change in algae cover, based on the fit of the Geometric Model to the data (see Section 2.2.6 for full technical details).

The maximum rate of change in algae cover (i.e. the rate of change in algae cover at the tipping point) was predicted to range between  $\approx 2$  to  $\approx 10$  % cover per day, depending on the data used to inform this estimate (Table 4). We note that the predicted maximum rate of change is lower for all side-oriented boulder surfaces than the corresponding top-oriented surfaces, consistent with previous results showing a difference between top- and side-oriented surfaces.

Table 4: Values predicted by the Geometric Model for the timing of the tipping point and value of the maximum rate of change in algae cover per day at this tipping point (mean  $\pm$  standard deviation, obtained from 1000 posterior samples) for the calibrated model. Note we did not consider any tipping point predictions for the Step Model or Linear Model as discussed in Sections 2.2.6.

Scenario	Maximum rate of change (% day <sup>-1</sup> )	Date
Top data, relative to all	6.8 $\pm$ 0.2	20 January $\pm$ 2 days
Top data, relative to nonabundant	10.1 $\pm$ 0.8	23 February $\pm$ 8 days
Top data, absolute	3.9 $\pm$ 0.4	28 February $\pm$ 3 days
Side data, relative to all	5.8 $\pm$ 0.3	8 January $\pm$ 3 days
Side data, relative to nonabundant	6.7 $\pm$ 0.2	18 January $\pm$ 1 day
Side data, absolute	1.9 $\pm$ 0.2	8 January $\pm$ 3 days

In four out of six scenarios, the Geometric Model predicted that the tipping point occurs in January, while in the remaining two scenarios, the tipping point was predicted to occur in February (Table 4, Figure 11). Interestingly, all predicted tipping points are predicted to fall later in the year than the summer solstice (compare red shaded region and black dashed line in Figure 11). This means that for a decreasing period of sea-ice cover, where the date of sea-ice break-out moves earlier in the year, these dates will be reached *before* the date of sea-ice break-out coincides with the summer solstice. Therefore, our work predicts that if the sea-ice breaks out earlier in the year

than the summer solstice (to the left of the black dashed line in Figure 11), the tipping point has already been passed, and the site is highly likely to be suitable for algae growth on both tops and sides of boulders.

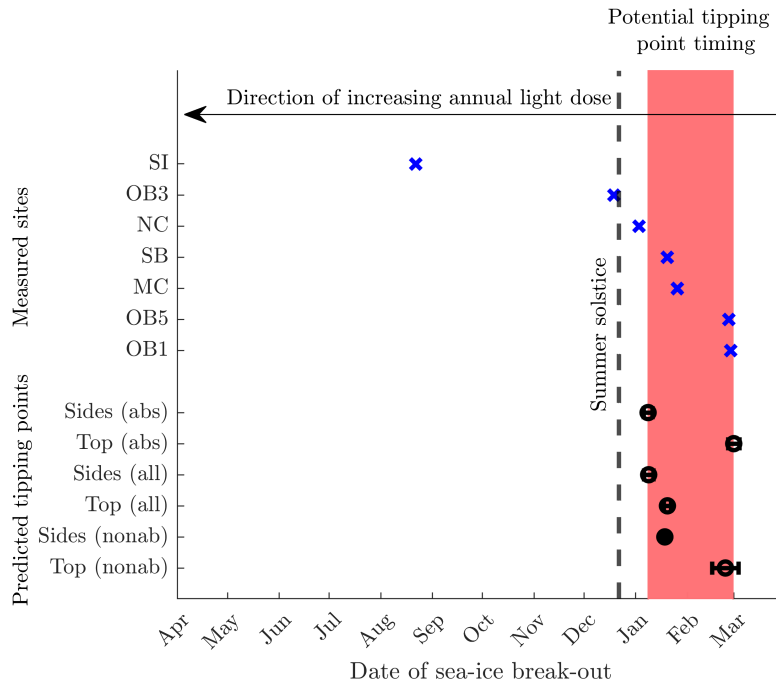


Figure 11: Comparison of measured sea-ice break-out dates for seven sites in the Windmill Islands against our predicted tipping point dates based on fitting energy-dependent sigmoid growth models to data from these sites. The blue crosses indicate the measured date of sea-ice break-out for each of the seven sites (discussed in Section 2.2.1). The black circles with error bars indicate the estimated date of sea-ice break-out ( $\pm$  standard deviation) at which the maximum rate of change in algae cover is reached, as a proxy for the date of the tipping point. Note we did not consider any tipping point predictions for the Step Model or Linear Model as discussed in Sections 2.2.6. In this figure, as the period of sea-ice cover decreases, the date of sea-ice break-out moves earlier in the year (i.e. from right to left). The date of the summer solstice is shown by the black dashed line. The red shaded region indicates the range of dates of sea-ice break-out within which the tipping point was predicted by our models. Our results indicate that the seven sites are either in the vicinity of, or have already passed, the tipping point.



## 4. Discussion

### 4.1. Model framework

In this work we have introduced and demonstrated a new model framework that can yield steady state populations with a nontrivial dependence on the energy available to the system, overcoming the issues with more traditional phenomenological modelling approaches described in Section 1. We have taken three model examples of this framework and shown how they fit with data from a case study system in Antarctica, confirming the models are capable of predicting key ecological parameters and tipping points, without the requirement for complex models with a large number of parameters.

While our work has focussed specifically on the model framework’s application to the Antarctic case study, we note it is general in nature and has a broad application to any system requiring a dependence on (some form of) energy. Its construction allows incorporation of many existing sigmoid growth models (discussed by Banks 1993) via modification of the crowding function  $f_c(N(t); K, \lambda)$ . The model framework’s generality also makes it flexible; it can be as coarse or detailed as required, and can easily be adapted to suit specific systems if desired, via modifications of the framework’s required functions  $f_c(N(t); K, \lambda)$ ,  $f_E(E; \lambda)$  and  $f_N(N(t); \lambda)$ .

However, we reiterate that this framework is only defined for a population  $N(t)$  satisfying  $0 \leq N(t) \leq K$ . While this is common in many biological and ecological systems, our framework may require modifications if it is to be applied to systems where this inequality does not hold. Care must also be taken to ensure the selections for  $f_c(N(t); K, \lambda)$ ,  $f_E(E; \lambda)$  and  $f_N(N(t); \lambda)$  avoid non-physical behaviour and adhere to the mathematical requirements set out in Section 2.1.

### 4.2. Choosing models from the framework for Antarctic algae

Of the three example models examined in this work, our results found that the Linear Model was the most suited for forecasting Antarctic benthic algae cover. The Linear Model was the best-performing model when fitting to the available data. We therefore suggest that the Linear Model

should be used for forecasting algae cover or determining the value of compensation irradiance  $E_c$ , which is a parameter that is biologically meaningful (Adams et al., 2017) as a metric of minimum light requirements for algae. However, if the desired application was to determine information (e.g. the date) about potential tipping points, the Geometric Model is better suited (see Section 2.2.6 for full details).

However, regardless of each of the three models' ability to represent Antarctic benthic algae, these models all have general merits and are likely to find a broad application in many other ecological contexts. Although the Step Model was generally not suitable for forecasting benthic algae cover or quantifying tipping points, we note this model could be used to represent any system where limited data is available to characterise the shape of the dependence of steady state populations on energy and/or systems that do not have a justification for usage of the more complicated Geometric Model. The Linear Model could similarly be applied to any system where steady state populations possessing linear dependence on energy (within a finite range of energy values) is an ideal first model to trial (i.e. in the absence of other mechanistic understanding). On the other hand, the Geometric Model (due to its geometric derivation from plant cover as a function of available light) provides a mechanistic understanding of benthic plant growth or cover in response to light, so is well suited for such applications.

### 4.3. Predicting the light requirements of Antarctic algae

We next turn our attention to the comparison of our data-calibrated models' predictions of key ecological parameters for Antarctic algae, starting with the compensation irradiance  $E_c$ . A range of photosynthetic parameters for different algal species were calculated experimentally by Clark et al. (2013a), including the minimum annual light balance (mALB) for four nonabundant algae species (Table 5). Focussing here on our best-fitting model (the Linear Model), which predicted values for the compensation irradiance  $E_c$  ranging from  $\approx 0.02$  to  $\approx 0.33$  mol m<sup>-2</sup> d<sup>-1</sup> (Table 3), this range finds reasonable agreement with the mALB values of 0.074–0.690 mol m<sup>-2</sup> d<sup>-1</sup> experimentally determined by Clark et al. (2013a). In particular, we found the predicted values of  $E_c$  from the Linear Model were more consistent with the minimum annual light dose for the algae

species *Desmarestia menziesii* ( $0.074 \text{ mol m}^{-2} \text{ d}^{-1}$ ). As our models do not distinguish between different algae species, this may mean that our data-calibrated Linear Model will predict algae growth to be more consistent with *Desmarestia menziesii* than other more light-sensitive species.

Table 5: Minimum annual light balance experimentally determined by Clark et al. (2013a) for the four nonabundant algae species. The equivalent daily light dose was obtained by calculating  $\text{mALB}/365$ . The resulting range between the minimum and maximum bounds is also shown.

Species	mALB ( $\text{mol m}^{-2} \text{ yr}^{-1}$ )	mALB/365 ( $\text{mol m}^{-2} \text{ d}^{-1}$ )
<i>Desmarestia menziesii</i>	27	0.074
<i>Himantothallus grandifolius</i>	216	0.592
<i>Iridaea cordata</i>	127	0.348
<i>Palmaria decipiens</i>	252	0.690
Range	27-252	0.074-0.690

Our results show that the estimated values for the compensation irradiance  $E_c$  (and for the Linear Model, the saturation irradiance  $E_{\text{sat}}$ ) are always lower for the top-oriented surfaces, compared to the corresponding side-oriented surfaces (Section 3.3). Physically, these differences make sense. Geometrically, the orientation of side-facing surfaces compared to available light results in a smaller effective area (that is, the fraction of the area covered by algae as viewed from above) than top-facing surfaces due to self shading (Baird et al., 2016, 2020). As a result, algae on side-oriented surfaces will absorb less light than top-oriented surfaces for the same amount of available light.

Light attenuation is another factor which may affect the amount or intensity of light delivered to different boulder surfaces (Mitchell et al., 1991; Deregibus et al., 2016; Stambler et al., 1997). Light attenuation can be different for different regions (Deregibus et al., 2016), but also for different depths in the water column (Stambler et al., 1997), whereby surfaces located at greater depths will receive less light. In the present work we were unable to explore the variations in the benthic community composition with depth due to the limitations of the data. We expect that depth could play a role in determining this composition, although the presence or absence of sea-ice likely remains the greatest control on light availability for Antarctic shallow-water benthic communities.

Finally, the physical characteristics of the surrounding environment must also be considered. The data obtained by Clark et al. (2013a) involves observations taken from various boulder surfaces;

due to the irregular nature of such surroundings, it is therefore possible that, particularly for the side-oriented surfaces, the sample sites will be shaded (or partially shaded) by other boulders or structures. For side-oriented boulder surfaces, shading could even be caused by the boulder from which the sample was obtained, particularly in circumstances where the side-oriented surface was not strictly perpendicular to the seabed.

#### **4.4. Predicting the maximum cover, and rate of change in cover, of Antarctic algae**

In our results, we also found that the maximum algae cover possible, also known as the carrying capacity  $K$ , was predicted to be approximately 25 to 35% (Section 3.3). Recalling that  $K$  was only estimated when interpreting the data as absolute values, and that for this data interpretation it is assumed there is a non-biological and constant process preventing the maximum cover from reaching 100%, these results could represent a plausible upper limit for benthic algae growing in the shallow waters around Antarctica. Potential processes for limiting the maximum algae cover could include, for example, ice scour from bodies of ice colliding with the sea floor and/or substrate (Barnes, 1999; Peck et al., 1999; Brown et al., 2004; Johnston et al., 2007; Smale et al., 2007; Barnes and Souster, 2011), whereby continual collisions repeatedly clear fauna prior to it reaching full cover, although it is not clear how frequently this process occurs (Barnes, 1999; Brown et al., 2004).

Our analysis of tipping points suggested that there are some sea-ice break-out dates that can yield a change in steady state algae cover of up to  $\approx 4\%$  absolute cover or up to  $\approx 10\%$  relative cover if the ice breaks out one day earlier (Table 4). It is important to note that these maximum rates of change in algae cover are a worst case scenario, although these predictions reflect how quickly the habitat suitability could change. If the maximum rate of  $\approx 10\%$  *relative* algae cover per day is compared to expected maximum rates of sea-ice decline of up to 5 days per year estimated elsewhere (Clark et al., 2013a; Barnes and Souster, 2011; Parkinson, 2004; Stammerjohn et al., 2008), these predictions together suggest that the habitat suitability for algae could possibly increase by  $\approx 50\%$  relative cover in a single year, if the maximum rates of sea-ice cover date and algae cover suitability

(due to the tipping point) temporally coincide. Similarly, if the maximum rate of  $\approx 4\%$  *absolute* algae cover per day were to coincide with the maximum rate of sea-ice decline of 5 days per year, this would suggest the habitat suitability could possibly increase from zero to near its maximum (25–35% absolute cover) in a single year. Hence, our results highlight the value of monitoring changes in the sea-ice break-out date, especially if this date is in the vicinity of the dates where the tipping point may occur (Table 4), if warning of a potential change in benthic community dominance between algae and invertebrates in shallow coastal waters of Antarctica is of interest.

#### **4.5. Extending steady state models of Antarctic algae cover to dynamic models**

We have made the assumption that the algae and invertebrate data collected by Clark et al. (2013a) were from populations that had stabilised in time. This may not be the case (Hastings et al., 2018); however, without regular cover data measured repeatedly over a period of time, we cannot make cover predictions, or even compare the data between sites, unless we make this assumption.

The models we introduce only require one additional parameter, the growth rate  $r$ , to be estimated so that the models become fully-parameterised dynamic models of algae cover. The inherent challenge with incorporating this parameter into the model is that these ecosystems are composed of unknown proportions of a varying number of algae species (Clayton, 1994) of different sizes and at different stages in their life cycles. Each species has a different growth rate (Johnston et al., 2007), which itself varies both between male and female gametophytes, and across the year (Wiencke, 1990a). However, regardless of these complexities, the fact that only one additional parameter (the growth rate  $r$ ) is required to transform our fitted steady state models into dynamic models suggests this is a logical research direction for future work.

## **5. Conclusion**

In this work, we have demonstrated a newly proposed model framework with many uses, including estimating key ecological parameters, forecasting steady state populations and predicting environ-

mentally relevant thresholds (in this case, tipping points). This work has focussed on a specific case study in Antarctica; however the framework is highly flexible and could be applied to any biological or ecological system where there is a dependence of the system state on the available energy in the form of nutrients or some other fundamental requirement.

## Software and data availability

The code used in this work was written in MATLAB (R2021b) and is available to download from the Figshare Repository <https://doi.org/10.6084/m9.figshare.25458229>. This code comprises 44 MATLAB code files which perform the analysis and produces the figures shown in this manuscript. Also included is a MATLAB data file containing results generated by the analysis (including the light time series datasets, estimated annual light doses, averaged algae data, model outputs and credible intervals).

The code, data files and model output files contained in this repository are sufficient to generate all results shown in the paper (including all of the results shown in the Supplementary Material). Additional data fed into the Sequential Monte Carlo algorithm to generate the posterior distributions are confidential and therefore have not been provided in this repository, but are available upon reasonable request.

## Declaration of competing interest

The authors declare that they have no known competing financial interests or personal relationships that could have appeared to influence the work in this paper.

## Acknowledgements

The authors thank Patrick Hassard, Sarika Karanth, Jonathan Stark, and Sarah Vollert for helpful discussions during preparation of this manuscript. ELM and GFC were supported by the Australian Research Council (ARC) SRIEAS Grant SR200100005 Securing Antarctica's Environmen-

tal Future. MPA's contribution was funded by an ARC Discovery Early Career Researcher Award DE200100683.

## References

- Abram, N.J., Thomas, E.R., McConnell, J.R., Mulvaney, R., Bracegirdle, T.J., Sime, L.C., Aris-tarain, A.J., 2010. Ice core evidence for a 20th century decline of sea ice in the Bellingshausen Sea, Antarctica. *Journal of Geophysical Research: Atmospheres* 115, D23101. doi:10.1029/2010JD014644.
- Acevedo, M.A., Marcano, M., Fletcher, R.J., 2012. A diffusive logistic growth model to describe forest recovery. *Ecological Modelling* 244, 13–19. doi:10.1016/j.ecolmodel.2012.07.012.
- Adams, M.P., Collier, C.J., Uthicke, S., Ow, Y.X., Langlois, L., O'Brien, K.R., 2017. Model fit versus biological relevance: Evaluating photosynthesis-temperature models for three tropical seagrass species. *Scientific Reports* 7. doi:10.1038/srep39930.
- Adams, M.P., Ghisalberti, M., Lowe, R.J., Callaghan, D.P., Baird, M.E., Infantes, E., O'Brien, K.R., 2018. Water residence time controls the feedback between seagrass, sediment and light: Implications for restoration. *Advances in Water Resources* 117, 14–26. doi:10.1016/j.advwatres.2018.04.004.
- Adams, M.P., Koh, E.J., Vilas, M.P., Collier, C.J., Lambert, V.M., Sisson, S.A., Quiroz, M., McDonald-Madden, E., McKenzie, L.J., O'Brien, K.R., 2020a. Predicting seagrass decline due to cumulative stressors. *Environmental Modelling & Software* 130, 104717. doi:10.1016/j.envsoft.2020.104717.
- Adams, M.P., Sisson, S.A., Helmstedt, K.J., Baker, C.M., Holden, M.H., Plein, M., Holloway, J., Mengersen, K.L., McDonald-Madden, E., 2020b. Informing management decisions for ecological networks, using dynamic models calibrated to noisy time-series data. *Ecology Letters* 23, 607–619. doi:10.1111/ele.13465.
- Allee, W.C., Bowen, E.S., 1932. Studies in animal aggregations: Mass protection against col-loidal silver among goldfishes. *Journal of Experimental Zoology* 61, 185–207. doi:10.1002/jez.1400610202.



- Baird, M.E., Adams, M.P., Babcock, R.C., Oubelkheir, K., Mongin, M., Wild-Allen, K.A., Skerratt, J., Robson, B.J., Petrou, K., Ralph, P.J., O'Brien, K.R., Carter, A.B., Jarvis, J.C., Rasheed, M.A., 2016. A biophysical representation of seagrass growth for application in a complex shallow-water biogeochemical model. *Ecological Modelling* 325, 13–27. doi:10.1016/j.ecolmodel.2015.12.011.
- Baird, M.E., Wild-Allen, K.A., Parslow, J., Mongin, M., Robson, B., Skerratt, J., Rizwi, F., Soja-*Woźniak*, M., Jones, E., Herzfeld, M., Margvelashvili, N., Andrewartha, J., Langlais, C., Adams, M.P., Cherukuru, N., Gustafsson, M., Hadley, S., Ralph, P.J., Rosebrock, U., Schroeder, T., Laiolo, L., Harrison, D., Steven, A.D.L., 2020. CSIRO Environmental Modelling Suite (EMS): scientific description of the optical and biogeochemical models (vB3p0). *Geoscientific Model Development* 13, 4503–4553. doi:10.5194/gmd-13-4503-2020.
- Banks, R.B., 1993. *Growth and Diffusion Phenomena: Mathematical Frameworks and Applications*. Springer Science & Business Media.
- Banner, K.M., Irvine, K.M., Rodhouse, T.J., 2020. The use of Bayesian priors in Ecology: The good, the bad and the not great. *Methods in Ecology and Evolution* 11, 882–889. doi:10.1111/2041-210X.13407.
- Barnes, D.K., 1999. The influence of ice on polar nearshore benthos. *Journal of the Marine Biological Association of the United Kingdom* 79, 401–407. doi:10.1017/S0025315498000514.
- Barnes, D.K.A., Souster, T., 2011. Reduced survival of Antarctic benthos linked to climate-induced iceberg scouring. *Nature Climate Change* 1, 365–368. doi:10.1038/nclimate1232.
- Brauer, F., 1979. Harvesting strategies for population systems. *The Rocky Mountain Journal of Mathematics* 9, 19–26. doi:10.1216/RMJ-1979-9-1-19.
- Brauer, F., Sánchez, D.A., 1975. Constant rate population harvesting: Equilibrium and stability. *Theoretical Population Biology* 8, 12–30. doi:10.1016/0040-5809(75)90036-2.

- Brown, K.M., Fraser, K.P.P., Barnes, D.K.A., Peck, L.S., 2004. Links between the structure of an Antarctic shallow-water community and ice-scour frequency. *Oecologia* 141, 121–129. doi:10.1007/s00442-004-1648-6.
- Browning, A.P., McCue, S.W., Simpson, M.J., 2017. A Bayesian computational approach to explore the optimal duration of a cell proliferation assay. *Bulletin of Mathematical Biology* 79, 1888–1906. doi:10.1007/s11538-017-0311-4.
- Browning, A.P., Warne, D.J., Burrage, K., Baker, R.E., Simpson, M.J., 2020. Identifiability analysis for stochastic differential equation models in systems biology. *Journal of The Royal Society Interface* 17, 20200652. doi:10.1098/rsif.2020.0652.
- Clark, G.F., Raymond, B., Riddle, M.J., Stark, J.S., Johnston, E.L., 2015. Vulnerability of Antarctic shallow invertebrate-dominated ecosystems. *Austral Ecology* 40, 482–491. doi:10.1111/aec.12237.
- Clark, G.F., Stark, J.S., Johnston, E.L., Runcie, J.W., Goldsworthy, P.M., Raymond, B., Riddle, M.J., 2013a. Light-driven tipping points in polar ecosystems. *Global Change Biology* 19, 3749–3761. doi:10.1111/gcb.12337.
- Clark, G.F., Stark, J.S., Johnston, E.L., Runcie, J.W., Goldsworthy, P.M., Raymond, B., Riddle, M.J., 2013b. Light-driven tipping points in polar ecosystems - Casey Station, Antarctica, Ver. 1. doi:10.4225/15/51D4D578E62B3.
- Clark, G.F., Stark, J.S., Palmer, A.S., Riddle, M.J., Johnston, E.L., 2017. The roles of sea-ice, light and sedimentation in structuring shallow Antarctic benthic communities. *PLOS ONE* 12, e0168391. doi:10.1371/journal.pone.0168391.
- Clayton, M.N., 1994. Evolution of the Antarctic marine benthic algal flora. *Journal of Phycology* 30, 897–904. doi:10.1111/j.0022-3646.1994.00897.x.
- Convey, P., Chown, S.L., Clarke, A., Barnes, D.K.A., Bokhorst, S., Cummings, V., Ducklow, H.W., Frati, F., Green, T.G.A., Gordon, S., Griffiths, H.J., Howard-Williams, C., Huiskes, A.H.L.,

- Laybourn-Parry, J., Lyons, W.B., McMinn, A., Morley, S.A., Peck, L.S., Quesada, A., Robinson, S.A., Schiaparelli, S., Wall, D.H., 2014. The spatial structure of Antarctic biodiversity. *Ecological Monographs* 84, 203–244. doi:10.1890/12-2216.1.
- Cooke, K.L., Witten, M., 1986. One-dimensional linear and logistic harvesting models. *Mathematical Modelling* 7, 301–340. doi:10.1016/0270-0255(86)90054-0.
- Corless, R.M., Gonnet, G.H., Hare, D.E.G., Jeffrey, D.J., Knuth, D.E., 1996. On the LambertW function. *Advances in Computational Mathematics* 5, 329–359. doi:10.1007/BF02124750.
- Dai, C., Heng, J., Jacob, P.E., Whiteley, N., 2022. An invitation to Sequential Monte Carlo samplers. *Journal of the American Statistical Association* 117, 1587–1600. doi:10.1080/01621459.2022.2087659.
- Dell, R.K., 1972. Antarctic Benthos, Academic Press. volume 10 of *Advances in Marine Biology*. chapter 1, pp. 1–216. doi:10.1016/S0065-2881(08)60416-2.
- Deregibus, D., Quartino, M.L., Campana, G.L., Momo, F.R., Wiencke, C., Zacher, K., 2016. Photosynthetic light requirements and vertical distribution of macroalgae in newly ice-free areas in Potter Cove, South Shetland Islands, Antarctica. *Polar Biology* 39, 153–166. doi:10.1007/s00300-015-1679-y.
- Dummermuth, A.L., Wiencke, C., 2003. Experimental investigation of seasonal development in six Antarctic red macroalgae. *Antarctic Science* 15, 449–457. doi:10.1017/S095410200300155X.
- Eagleson, P.S., 2002. *Ecohydrology: Darwinian Expression of Vegetation Form and Function*. Cambridge University Press. doi:10.1017/CB09780511535680.
- Erfteimeijer, P.L., Robin Lewis, R.R., 2006. Environmental impacts of dredging on seagrasses: a review. *Marine Pollution Bulletin* 52, 1553–1572. doi:10.1016/j.marpolbul.2006.09.006.
- Fadai, N.T., Simpson, M.J., 2020. Population dynamics with threshold effects give rise to a diverse family of Allee effects. *Bulletin of Mathematical Biology* 82, 74. doi:10.1007/s11538-020-00756-5.

- Fisher, J.C., Pry, R.H., 1971. A simple substitution model of technological change. *Technological Forecasting and Social Change* 3, 75–88. doi:10.1016/S0040-1625(71)80005-7.
- Girolami, M., 2008. Bayesian inference for differential equations. *Theoretical Computer Science* 408, 4–16. doi:10.1016/j.tcs.2008.07.005.
- Gómez, I., Wiencke, C., 1997. Seasonal growth and photosynthetic performance of the Antarctic macroalga *Desmarestia menziesii* (Phaeophyceae) cultivated under fluctuating Antarctic daylengths. *Botanica Acta* 110, 25–31. doi:s10.1111/j.1438-8677.1997.tb00607.x.
- Griffiths, H.J., 2010. Antarctic marine biodiversity – what do we know about the distribution of life in the Southern Ocean? *PLOS ONE* 5, e11683. doi:10.1371/journal.pone.0011683.
- Grozdanovski, T., Shepherd, J.J., Stacey, A., 2009. Multi-scaling analysis of a logistic model with slowly varying coefficients. *Applied Mathematics Letters* 22, 1091–1095. doi:10.1016/j.aml.2008.10.002.
- Hastings, A., Abbott, K.C., Cuddington, K., Francis, T., Gellner, G., Lai, Y.C., Morozov, A., Petrovskii, S., Scranton, K., Zeeman, M.L., 2018. Transient phenomena in ecology. *Science* 361, eaat6412. doi:10.1126/science.aat6412.
- Holling, C.S., 1973. Resilience and stability of ecological systems. *Annual Review of Ecology and Systematics* 4, 1–23. doi:10.1146/annurev.es.04.110173.000245.
- Idlango, M.A., Shepherd, J.J., Gear, J.A., 2017. Logistic growth with a slowly varying Holling type II harvesting term. *Communications in Nonlinear Science and Numerical Simulation* 49, 81–92. doi:10.1016/j.cnsns.2017.02.005.
- Idlango, M.A., Shepherd, J.J., Nguyen, L., Gear, J.A., 2012. Harvesting a logistic population in a slowly varying environment. *Applied Mathematics Letters* 25, 81–87. doi:10.1016/j.aml.2011.07.015.
- IUCN-CEM, 2022. The IUCN Red List of Ecosystems. Version 2022-1. URL: <https://assessments.iucnrle.org/assessments/13>.

- Jin, W., Penington, C.J., McCue, S.W., Simpson, M.J., 2016. Stochastic simulation tools and continuum models for describing two-dimensional collective cell spreading with universal growth functions. *Physical Biology* 13, 056003. doi:10.1088/1478-3975/13/5/056003.
- Johnson, J.B., Omland, K.S., 2004. Model selection in ecology and evolution. *Trends in Ecology & Evolution* 19, 101–108. doi:10.1016/j.tree.2003.10.013.
- Johnston, E.L., Connell, S.D., Irving, A.D., Pile, A.J., Gillanders, B.M., 2007. Antarctic patterns of shallow subtidal habitat and inhabitants in Wilke’s Land. *Polar Biology* 30, 781–788. doi:10.1007/s00300-006-0237-z.
- Katlein, C., Arndt, S., Nicolaus, M., Perovich, D.K., Jakuba, M.V., Suman, S., Elliott, S., Whitcomb, L.L., McFarland, C.J., Gerdes, R., Boetius, A., German, C.R., 2015. Influence of ice thickness and surface properties on light transmission through Arctic sea ice. *Journal of Geophysical Research: Oceans* 120, 5932–5944. doi:10.1002/2015JC010914.
- Kennicutt, M.C., Chown, S.L., Cassano, J.J., Liggett, D., Massom, R., Peck, L.S., Rintoul, S.R., Storey, J.W.V., Vaughan, D.G., Wilson, T.J., Sutherland, W.J., 2014. Polar research: six priorities for Antarctic science. *Nature* 512, 23–25. doi:10.1038/512023a.
- Knott, N., Underwood, A., Chapman, M., Glasby, T., 2004. Epibiota on vertical and on horizontal surfaces on natural reefs and on artificial structures. *Journal of the Marine Biological Association of the United Kingdom* 84, 1117–1130. doi:10.1017/S0025315404010550h.
- Koerich, G., Fraser, C.I., Lee, C.K., Morgan, F.J., Tonkin, J.D., 2023. Forecasting the future of life in Antarctica. *Trends in Ecology & Evolution* 38, 24–34. doi:10.1016/j.tree.2022.07.009.
- Kortsch, S., Primicerio, R., Beuchel, F., Renaud, P.E., Rodrigues, J., Lønne, O.J., Gulliksen, B., 2012. Climate-driven regime shifts in Arctic marine benthos. *Proceedings of the National Academy of Sciences* 109, 14052–14057. doi:10.1073/pnas.1207509109.
- Krause-Jensen, D., Marbà, N., Olesen, B., Sejr, M.K., Christensen, P.B., Rodrigues, J., Renaud, P.E., Balsby, T.J.S., Rysgaard, S., 2012. Seasonal sea ice cover as principal driver of spatial

- and temporal variation in depth extension and annual production of kelp in Greenland. *Global Change Biology* 18, 2981–2994. doi:10.1111/j.1365-2486.2012.02765.x.
- Mayewski, P.A., Meredith, M.P., Summerhayes, C.P., Turner, J., Worby, A., Barrett, P.J., Casassa, G., Bertler, N.A.N., Bracegirdle, T., Naveira Garabato, A.C., Bromwich, D., Campbell, H., Hamilton, G.S., Lyons, W.B., Maasch, K.A., Aoki, S., Xiao, C., van Ommen, T., 2009. State of the Antarctic and Southern Ocean climate system. *Reviews of Geophysics* 47, RG1003. doi:10.1029/2007RG000231.
- Miller, R.J., Etter, R.J., 2008. Shading facilitates sessile invertebrate dominance in the rocky subtidal Gulf of Maine. *Ecology* 89, 452–462. doi:10.1890/06-1099.1.
- Mitchell, B.G., Brody, E.A., Holm-Hansen, O., McClain, C., Bishop, J., 1991. Light limitation of phytoplankton biomass and macronutrient utilization in the southern ocean. *Limnology and Oceanography* 36, 1662–1677. doi:10.4319/lo.1991.36.8.1662.
- Murphy, E.J., Johnston, N.M., Hofmann, E.E., Phillips, R.A., Jackson, J.A., Constable, A.J., Henley, S.F., Melbourne-Thomas, J., Trebilco, R., Cavanagh, R.D., Tarling, G.A., Saunders, R.A., Barnes, D.K.A., Costa, D.P., Corney, S.P., Fraser, C.I., Höfer, J., Hughes, K.A., Sands, C.J., Thorpe, S.E., Trathan, P.N., Xavier, J.C., 2021. Global connectivity of Southern Ocean ecosystems. *Frontiers in Ecology and Evolution* 9, 624451. doi:10.3389/fevo.2021.624451.
- Murray, J.D., 1989. *Mathematical Biology*. Springer Berlin Heidelberg. doi:<https://doi.org/10.1007/b98868>.
- Noy-Meir, I., 1975. Stability of grazing systems: an application of predator-prey graphs. *Journal of Ecology* 63, 459–481. doi:10.2307/2258730.
- Parkinson, C.L., 2004. Southern Ocean sea ice and its wider linkages: insights revealed from models and observations. *Antarctic Science* 16, 387–400. doi:10.1017/S0954102004002214.
- Peck, L.S., 2018. *Oceanography and Marine Biology*. Taylor & Francis. chapter 3 Antarctic Marine Biodiversity. doi:10.1201/9780429454455.

- Peck, L.S., Brockington, S., Vanhove, S., Beghyn, M., 1999. Community recovery following catastrophic iceberg impacts in a soft-sediment shallow-water site at Signy Island, Antarctica. *Marine Ecology Progress Series* 186, 1–8. doi:10.3354/meps186001.
- Picken, G.B., 1985. Antarctica. Pergamon Press. chapter 4b Marine Habitats - Benthos. pp. 154–172.
- Purich, A., Doddridge, E.W., 2023. Record low Antarctic sea ice coverage indicates a new sea ice state. *Communications Earth & Environment* 4, 314. doi:10.1038/s43247-023-00961-9.
- Quartino, M.L., Deregibus, D., Campana, G.L., Latorre, G.E.J., Momo, F.R., 2013. Evidence of macroalgal colonization on newly ice-free areas following glacial retreat in Potter Cove (South Shetland Islands), Antarctica. *PLOS ONE* 8, e58223. doi:10.1371/journal.pone.0058223.
- Runcie, J.W., Riddle, M.J., 2006. Photosynthesis of marine macroalgae in ice-covered and ice-free environments in East Antarctica. *European Journal of Phycology* 41, 223–233. doi:10.1080/09670260600645824.
- Scheffer, M., Carpenter, S., Foley, J.A., Folke, C., Walker, B., 2001. Catastrophic shifts in ecosystems. *Nature* 413, 591–596. doi:10.1038/35098000.
- Scherrer, K.J.N., Kortsch, S., Varpe, Ø., Weyhenmeyer, G.A., Gulliksen, B., Primicerio, R., 2019. Mechanistic model identifies increasing light availability due to sea ice reductions as cause for increasing macroalgae cover in the Arctic. *Limnology and Oceanography* 64, 330–341. doi:10.1002/lno.11043.
- Shepherd, J.J., Stacey, A., Grozdanovski, T., 2012. Analysis of the power law logistic population model with slowly varying coefficients. *Mathematical Methods in the Applied Sciences* 35, 238–248. doi:10.1002/mma.1561.
- Simpson, M.J., Browning, A.P., Warne, D.J., Maclaren, O.J., Baker, R.E., 2022. Parameter identifiability and model selection for sigmoid population growth models. *Journal of Theoretical Biology* 535, 110998. doi:10.1016/j.jtbi.2021.110998.

- Smale, D.A., Barnes, D.K.A., Fraser, K.P.P., 2007. The influence of ice scour on benthic communities at three contrasting sites at Adelaide Island, Antarctica. *Austral Ecology* 32, 878–888. doi:10.1111/j.1442-9993.2007.01776.x.
- Stambler, N., Lovengreen, C., Tilzer, M.M., 1997. The underwater light field in the Bellingshausen and Amundsen Seas (Antarctica). *Hydrobiologia* 344, 41–56. doi:10.1023/A:1002993925441.
- Stammerjohn, S., Massom, R., Rind, D., Martinson, D., 2012. Regions of rapid sea ice change: an inter-hemispheric seasonal comparison. *Geophysical Research Letters* 39, L06501. doi:10.1029/2012GL050874.
- Stammerjohn, S.E., Martinson, D.G., Smith, R.C., Yuan, X., Rind, D., 2008. Trends in Antarctic annual sea ice retreat and advance and their relation to El Niño–Southern Oscillation and Southern Annular Mode variability. *Journal of Geophysical Research: Oceans* 113, C03S90. doi:10.1029/2007JC004269.
- Taylor, C.M., Hastings, A., 2005. Allee effects in biological invasions. *Ecology Letters* 8, 895–908. doi:10.1111/j.1461-0248.2005.00787.x.
- Thornley, J.M., 1990. A new formulation of the logistic growth equation and its application to leaf area growth. *Annals of Botany* 66, 309–311. doi:10.1093/oxfordjournals.aob.a088029.
- Tredennick, A.T., Hooker, G., Ellner, S.P., Adler, P.B., 2021. A practical guide to selecting models for exploration, inference, and prediction in ecology. *Ecology* 102, e03336. doi:10.1002/ecy.3336.
- Tsoularis, A., Wallace, J., 2002. Analysis of logistic growth models. *Mathematical Biosciences* 179, 21–55. doi:10.1016/S0025-5564(02)00096-2.
- Turschwell, M.P., Connolly, S.R., Schäfer, R.B., De Laender, F., Campbell, M.D., Mantyka-Pringle, C., Jackson, M., Kattwinkel, M., Sievers, M., Ashauer, R., Côté, I.M., Connolly, R.M., van den Brink, P.J., Brown, C., 2022. Interactive effects of multiple stressors vary with consumer interactions, stressor dynamics and magnitude. *Ecology Letters* 25, 1483–1496. doi:10.1111/ele.14013.



- Vilas, M., Bennett, F., Verburg, K., Adams, M., 2021. Considering unknown uncertainty in imperfect models: nitrogen mineralization as a case study, in: Vervoort, R., Voinov, A., Evans, J., Marshall, L. (Eds.), Proceedings of the 24th International Congress on Modelling and Simulation (MODSIM2021). Modelling and Simulation Society of Australia and New Zealand Inc. (MSSANZ), Australia, pp. 120–126. URL: <https://eprints.qut.edu.au/227108/>.
- Wang, M.H., Kot, M., Neubert, M.G., 2002. Integrodifference equations, Allee effects, and invasions. *Journal of Mathematical Biology* 44, 150–168. doi:10.1007/s002850100116.
- Warne, D.J., Baker, R.E., Simpson, M.J., 2019. Using experimental data and information criteria to guide model selection for reaction-diffusion problems in mathematical biology. *Bulletin of Mathematical Biology* 81, 1760–1804. doi:10.1007/s11538-019-00589-x.
- White, C., Marshall, D., 2019. Should we care if models are phenomenological or mechanistic? *Trends in Ecology and Evolution* 34, 276–278. doi:10.1016/j.tree.2019.01.006.
- Wiencke, C., 1990a. Seasonality of brown macroalgae from Antarctica—a long-term culture study under fluctuating Antarctic daylengths. *Polar Biology* 10, 589–600. URL: <https://doi.org/10.1007/BF00239370>, doi:10.1007/BF00239370.
- Wiencke, C., 1990b. Seasonality of red and green macroalgae from Antarctica—a long-term culture study under fluctuating Antarctic daylengths. *Polar Biology* 10, 601–607. doi:10.1007/BF00239371.
- World Health Organization, Food and Agriculture Organization of the United Nations, United Nations University, 2004. Human energy requirements: report of a joint FAO/WHO/UNU Expert Consultation. Technical Report.

# A generalised sigmoid population growth model with energy dependence: application to quantify the tipping point for Antarctic shallow seabed algae

## Supplementary Material

Elise Mills<sup>a,b,c,\*</sup>, Graeme F. Clark<sup>d,e,f</sup>, Matthew J. Simpson<sup>b</sup>, Mark Baird<sup>g</sup>, Matthew P. Adams<sup>a,b,c,h</sup>

<sup>a</sup>*Securing Antarctica's Environmental Future, Queensland University of Technology, Brisbane, 4001, QLD, Australia*

<sup>b</sup>*School of Mathematical Sciences, Queensland University of Technology, Brisbane, 4000, QLD, Australia*

<sup>c</sup>*Centre for Data Science, Queensland University of Technology, Brisbane, 4000, QLD, Australia*

<sup>d</sup>*Evolution & Ecology Research Centre, University of New South Wales, Sydney, 2052, NSW, Australia*

<sup>e</sup>*Centre of Marine Science and Innovation, University of New South Wales, Sydney, 2052, NSW, Australia*

<sup>f</sup>*School of Life and Environmental Sciences, University of Sydney, Camperdown, 2006, NSW, Australia*

<sup>g</sup>*CSIRO Oceans and Atmosphere, Hobart, 7001, TAS, Australia*

<sup>h</sup>*School of Chemical Engineering, The University of Queensland, St Lucia, 4072, QLD, Australia*

## S1. Approximating the annual light dose

In Section 3.2, we described our method for approximating the annual light dose for sea-ice break-out dates ranging from 2 April (1 day of ice cover) to 31 March the following year (365 days of ice cover). Figure S1.1 shows the *daily* measured light dose at each of the seven sites (red lines), as well as the daily light dose approximated using the process set out in Section 3.2 (blue lines). We consider these approximations are a reasonable representation of measured daily light values at each site and therefore this method can be used to adequately approximate the daily light dose (and therefore annual light dose) for the range of sea-ice break-out dates described above.

---

\*Corresponding Author

*Email addresses:* [elise.mills@qut.edu.au](mailto:elise.mills@qut.edu.au) (Elise Mills), [graeme.clark@sydney.edu.au](mailto:graeme.clark@sydney.edu.au) (Graeme F. Clark), [matthew.simpson@qut.edu.au](mailto:matthew.simpson@qut.edu.au) (Matthew J. Simpson), [mark.baird@csiro.au](mailto:mark.baird@csiro.au) (Mark Baird), [mp.adams@qut.edu.au](mailto:mp.adams@qut.edu.au) (Matthew P. Adams)

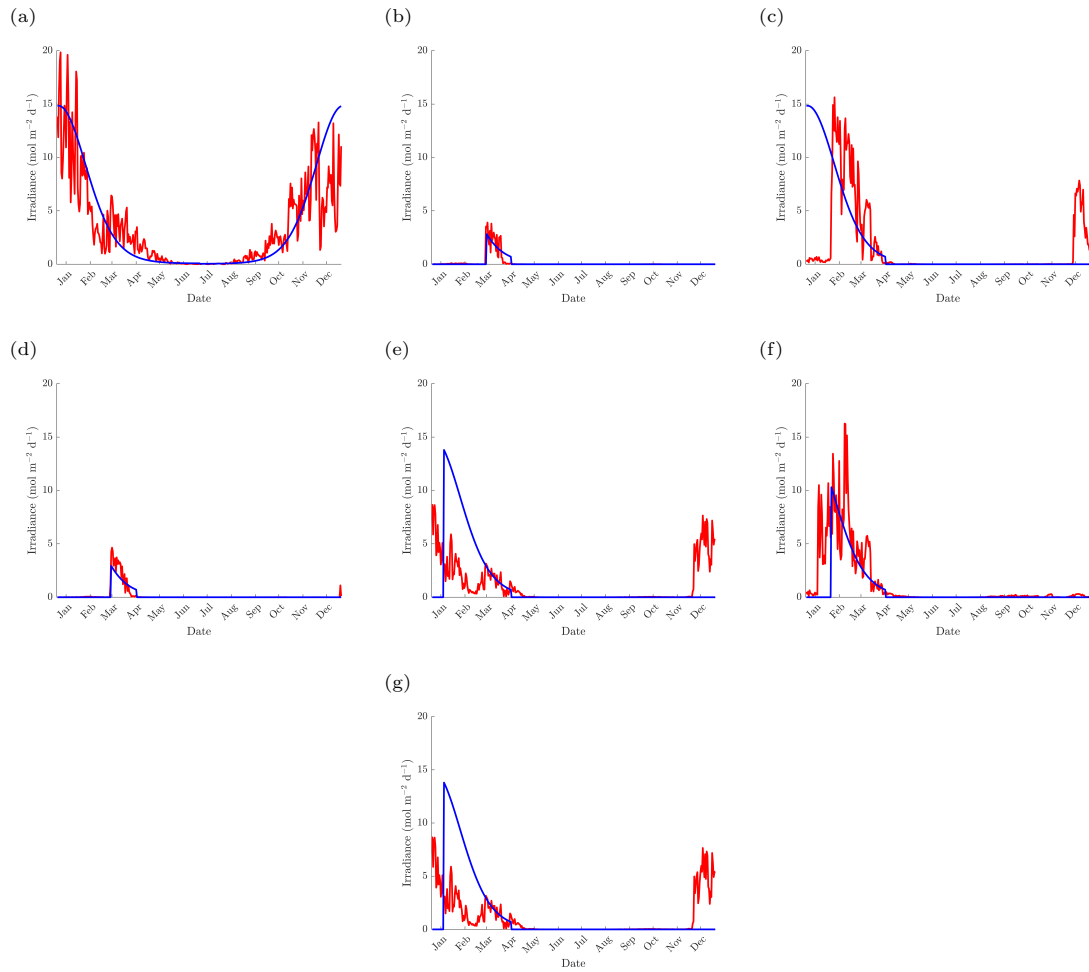


Figure S1.1: Daily measured light values (red) for each site in the study by Clark et al. (2013): (a) Shirley Island, (b) O'Brien Bay 1, (c) O'Brien Bay 3, (d) O'Brien Bay 5, (e) Newcomb Corner, (f) Shannon Bay and (g) McGrady Cove. Each subfigure shows the simulated light representative of each site (blue) implemented by replacing the values modelled by Clark et al. (2013) with  $E = 0 \text{ mol m}^{-2} \text{ d}^{-1}$  to represent ice cover.

## S2. Mathematical artefacts of the Linear Model when predicting the tipping point

Our preliminary results showed that for the Linear Model, in five out of six scenarios, the tipping point was predicted to occur once the period of sea-ice cover decreased such that the date of sea-ice break-out fell between 22 and 28 December. These dates are consistent with the maximum daily light modelled by Clark et al. (2013) occurring on the summer solstice, which falls on 22-23 December (Figure 6), accounting for the uncertainty in parameter predictions. We note these results are an artefact of the functional form of the Linear Model, as follows.

**Summary:** If the algae population cover linearly scales with available light, and  $E_{\text{sol}}$  (defined here as the annual light dose when the date of sea-ice break-out reaches the summer solstice) falls within the range of  $E_c$  and  $E_{\text{sat}}$ , the tipping point will *always* be predicted to occur at the summer solstice, as this is the date when the sea-ice break-out timing has the greatest effect on the annual light dose (Figure S2.1, also see Figure 7). If  $E_{\text{sat}} < E_{\text{sol}}$ , the date on which the annual light dose is closest to  $E_{\text{sat}}$  will be selected as the timing of the tipping point, as this is the date when the sea-ice break-out timing causes the greatest change to steady state algae cover given the constraints of  $E_c$  and  $E_{\text{sat}}$ .

**Further explanation:** Mathematically, the rate of change in algae cover with respect to the date of sea-ice break-out can be expressed via the chain rule:

$$\frac{dN}{dt_{\text{break-out}}} = \frac{dN}{dE_{\text{annual}}} \frac{dE_{\text{annual}}}{dt_{\text{break-out}}}. \quad (\text{S2.1})$$

We note that when  $E_{\text{annual}} < E_c$  and  $E_{\text{annual}} > E_{\text{sat}}$ , there is no change in algae cover; however within the range  $E_c < E_{\text{annual}} < E_{\text{sat}}$ , the model describes a strictly linear increase in algae cover (see Figure 3). This therefore means that when  $E_c < E_{\text{annual}} < E_{\text{sat}}$ , the rate of change in algae cover with respect to the date of sea-ice break-out is proportional to the rate of change in the annual

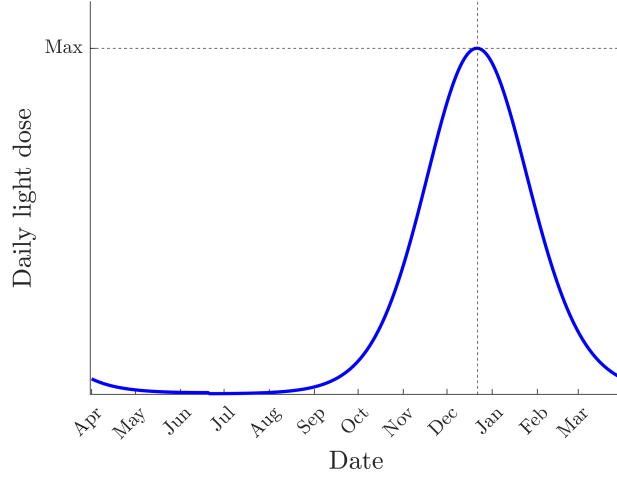


Figure S2.1: This figure shows the daily light dose for each day throughout the year, starting from 1 April through to 31 March the following year. The vertical dashed line shows the approximate date of the summer solstice (22-23 December). It is clear the maximum daily light dose occurs on the summer solstice; this date will have the greatest effect on the annual light dose.

light dose with respect to the date of sea-ice break-out:

$$\frac{dN}{dt_{\text{break-out}}} = \kappa \frac{dE_{\text{annual}}}{dt_{\text{break-out}}}, \quad (\text{S2.2})$$

where  $\kappa$  is a constant. This means that the maximum rate of change in algae cover occurs when the maximum rate of change in the annual light dose occurs, within the range of  $E_{\text{sat}} > E_{\text{annual}} > E_c$ . In contrast, the constant  $\kappa$  changes to zero if  $E_{\text{annual}} < E_c$  or  $E_{\text{annual}} > E_{\text{sat}}$  due to the steady state behaviour of the Linear Model (see Figure 3). Hence, for the Linear Model, the tipping point can only occur for annual light doses  $E_{\text{annual}}$  between  $E_c$  and  $E_{\text{sat}}$ .

Figure S2.2 shows the rate of change in algae cover for the two cases mentioned previously: when  $E_{\text{sat}} > E_{\text{sol}} > E_c$  (Figure S2.2a), and when  $E_{\text{sol}} > E_{\text{sat}} > E_c$  (Figure S2.2b). As the algae cover only changes between the irradiance values of  $E_c$  and  $E_{\text{sat}}$ , the cover only changes between the *dates* on which these irradiance values are reached. When  $E_{\text{sat}} > E_{\text{sol}} > E_c$ , it is clear that the maximum rate of change in algae cover will occur at the summer solstice, as this is when the maximum rate of change in the annual light dose occurs. However when  $E_{\text{sol}} > E_{\text{sat}} > E_c$ , the

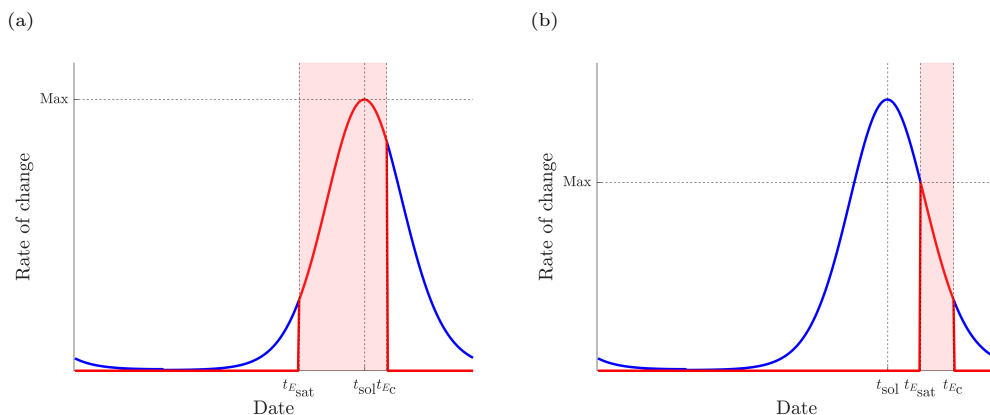


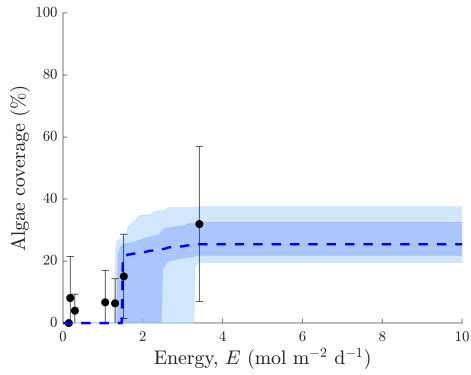
Figure S2.2: This figure shows the relationship between the daily light dose (blue lines, also representing the rate of change in the annual light dose), scaled rate of change of algae cover (red lines, with  $\kappa$  from Equation S2.2 set to 1 for illustrative purposes) and the date. The vertical lines show the dates on which the annual light dose reaches the compensation irradiance  $E_c$  (date  $t_{E_c}$ ) the saturation irradiance  $E_{\text{sat}}$  (date  $t_{E_{\text{sat}}}$ ), and the date of the summer solstice (date  $t_{\text{sol}}$ ). The red shaded regions represent the dates of sea-ice break-out where the annual light dose is between  $E_c$  and  $E_{\text{sat}}$  (between the dates  $t_{E_c}$  and  $t_{E_{\text{sat}}}$ ). Figure S2.2a shows what happens when  $t_{\text{sol}}$  is between  $t_{E_c}$  and  $t_{E_{\text{sat}}}$  ( $E_{\text{sat}} > E_{\text{sol}} > E_c$ ), while Figure S2.2b shows what happens when  $t_{\text{sol}}$  is outside of that range ( $E_{\text{sol}} > E_{\text{sat}} > E_c$ ). It is clear that in the first case ( $E_{\text{sat}} > E_{\text{sol}} > E_c$ ),  $t_{\text{sol}}$  is within the range of dates where a change in algae cover with date of sea-ice break-out is predicted by the Linear Model, and therefore the maximum rate of change occurs at  $t_{\text{sol}}$ , when the maximum daily light is reached. However in the second case ( $E_{\text{sat}} > E_{\text{sol}} > E_c$ ),  $t_{\text{sol}}$  is no longer within the range of dates where a change in algae cover with date of sea-ice break-out is predicted by the Linear Model, and instead the maximum rate of change occurs on the closest date to  $t_{E_{\text{sol}}}$  that does fall within that range of dates; this closest date will be  $t_{E_{\text{sat}}}$ .

maximum rate of change of the annual light dose occurs outside of the range  $E_{\text{sat}} > E_{\text{annual}} > E_c$  and therefore when algae cover is constant. So, instead, it is clear from Figure S2.2b that the rate of change in algae cover within  $E_c < E_{\text{annual}} < E_{\text{sat}}$  increases as the date of sea-ice break-out moves earlier in the year while approaching the summer solstice, and therefore the maximum rate of change in algae cover will occur on the date on which the annual light dose is closest in value to  $E_{\text{sat}}$ .

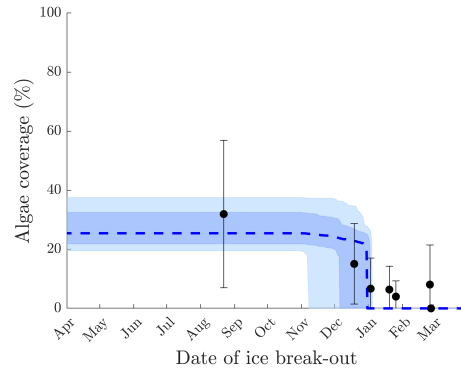
### S3. Additional model-data fits

Together with Figure 8f, the figures in this section show the fit of each model to the data for each of the six scenarios (see Table 3). Specifically, these plots show the forecasted algae cover for different values of annual light dose values  $E$  ( $\text{mol m}^{-2} \text{d}^{-1}$ ), and for different dates of sea-ice break-out; with the latter assuming that the light received by algae in absence of ice coverage follows the modelled light dose fitted to data for Shirley Island (blue line in Figure 6). The median model predictions are shown by the dashed lines, the 68% credible intervals are shown by the dark blue shaded regions, and the 95% credible intervals are shown by the light blue shaded regions. The forecasts are compared to the data obtained by Clark et al. (2013), shown in black. These forecasts represent habitat suitability, and we note this quantity is still limited by available light.

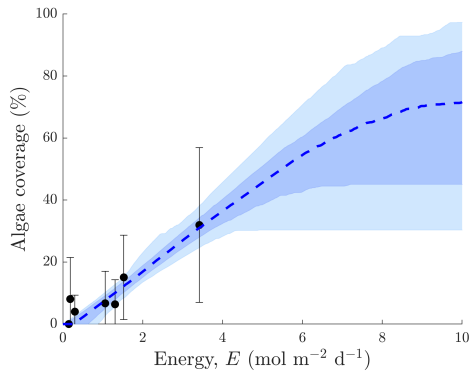
(a) Step Model, algae cover vs light dose



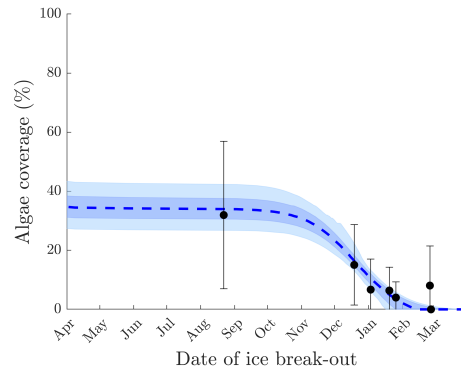
(b) Step Model, algae cover vs sea-ice break-out date



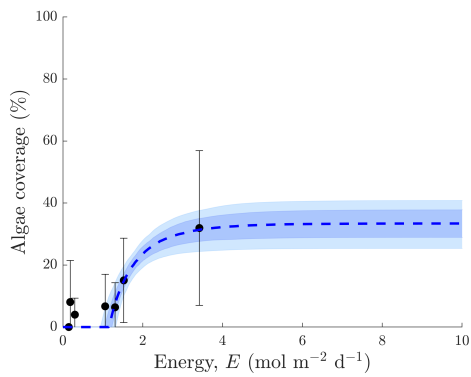
(c) Linear Model, algae cover vs light dose



(d) Linear Model, algae cover vs sea-ice break-out date



(e) Geometric Model, algae cover vs light dose



(f) Geometric Model, algae cover vs sea-ice break-out date

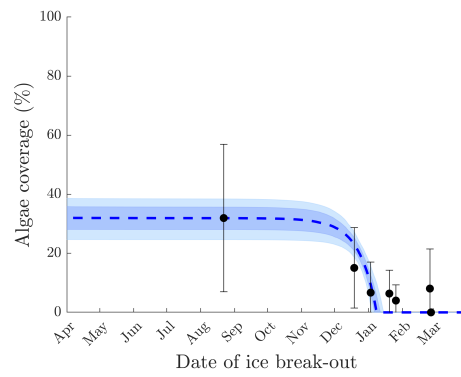


Figure S3.1: Model-data fits for side-oriented surfaces of boulders, interpreting the data as absolute values. (See caption of Figure 8 for further details.)



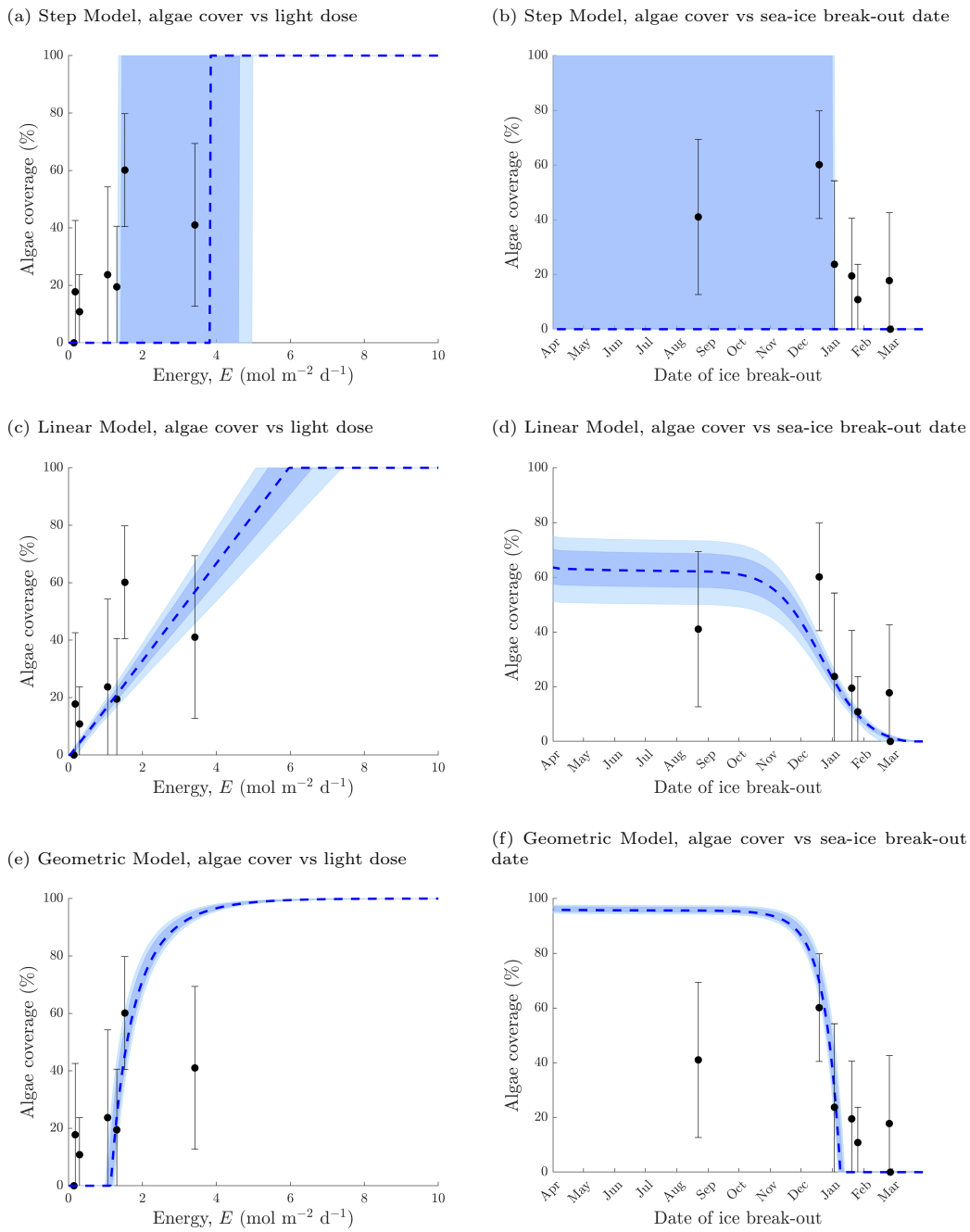
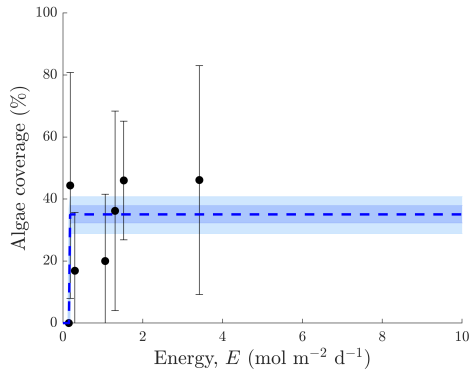
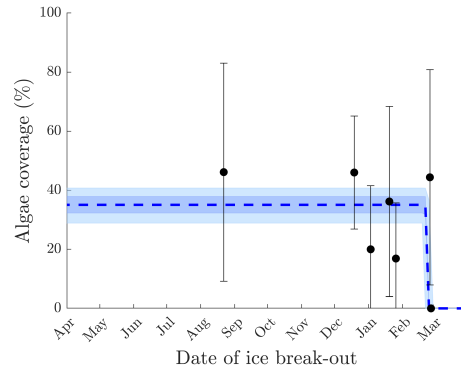


Figure S3.2: Model-data fits for side-oriented surfaces of boulders, interpreting the data as relative to the cumulative cover of invertebrates and algae. (See caption of Figure 8 for further details.) This particular example highlights the high degree of uncertainty involved in the predictions for the Step Model.

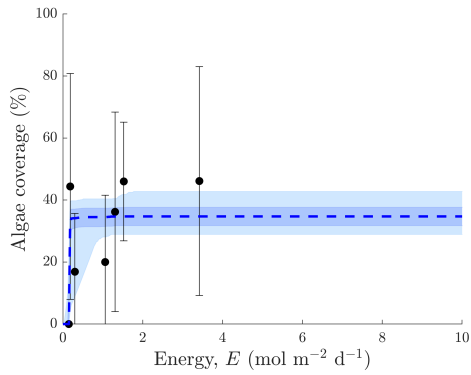
(a) Step Model, algae cover vs light dose



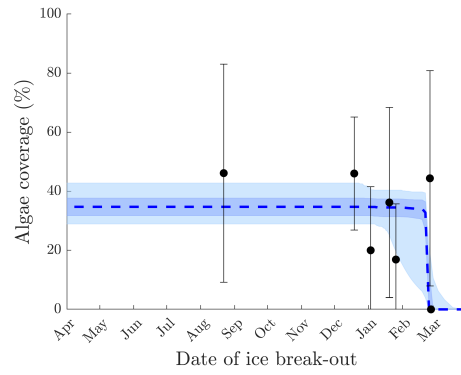
(b) Step Model, algae cover vs sea-ice break-out date



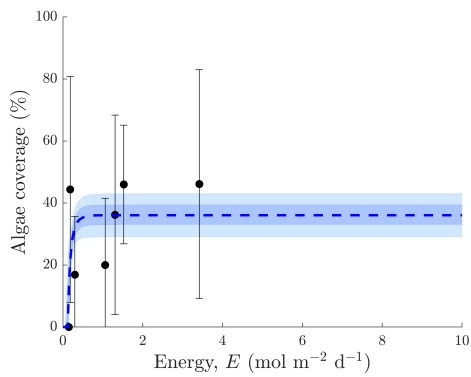
(c) Linear Model, algae cover vs light dose



(d) Linear Model, algae cover vs sea-ice break-out date



(e) Geometric Model, algae cover vs light dose



(f) Geometric Model, algae cover vs sea-ice break-out date

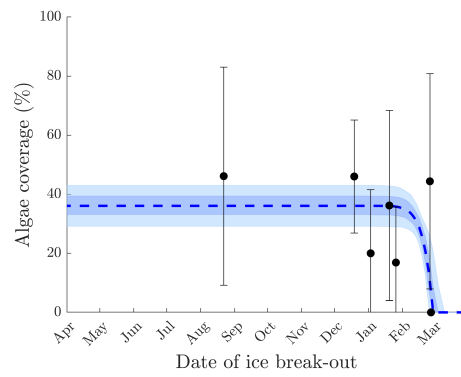
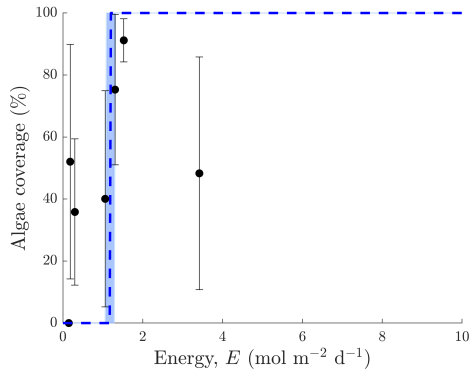
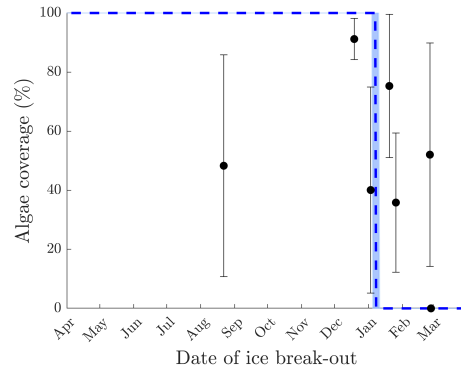


Figure S3.3: Model-data fits for top-oriented surfaces of boulders, interpreting the data as absolute values. (See caption of Figure 8 for further details.)

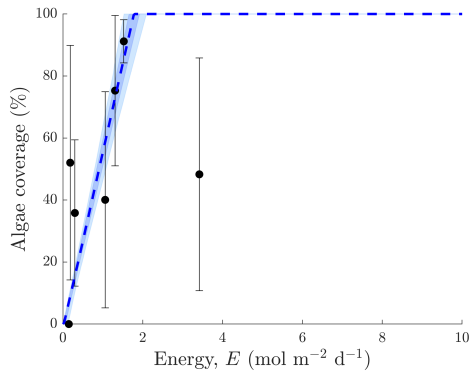
(a) Step Model, algae cover vs light dose



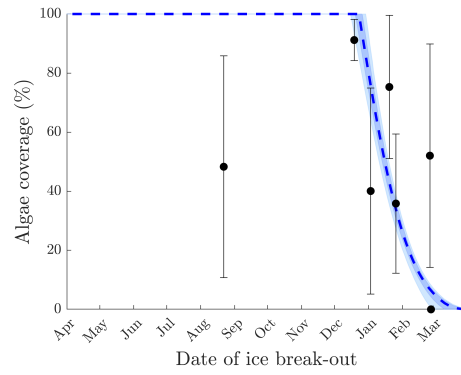
(b) Step Model, algae cover vs sea-ice break-out date



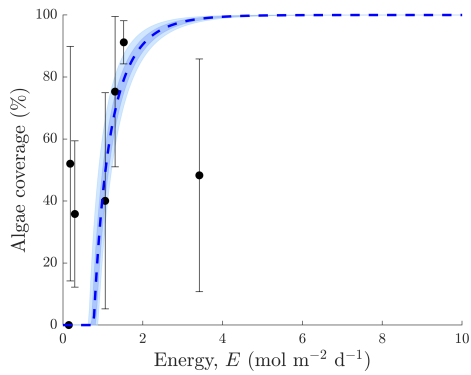
(c) Linear Model, algae cover vs light dose



(d) Linear Model, algae cover vs sea-ice break-out date



(e) Geometric Model, algae cover vs light dose



(f) Geometric Model, algae cover vs sea-ice break-out date

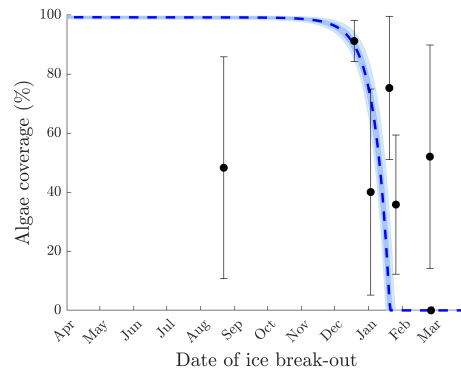
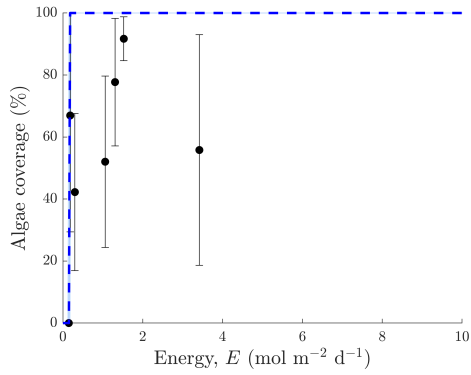
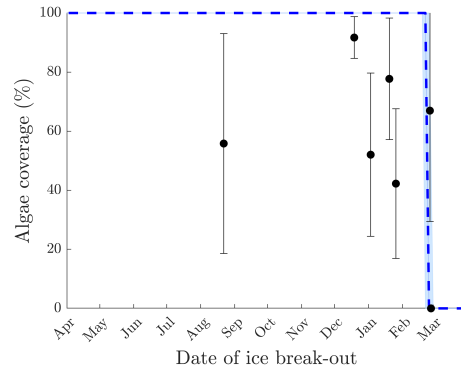


Figure S3.4: Model-data fits for top-oriented surfaces of boulders, interpreting the data as relative to the cumulative cover of invertebrates and algae. (See caption of Figure 8 for further details.)

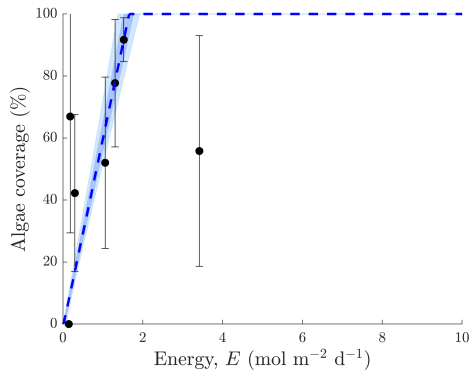
(a) Step Model, algae cover vs light dose



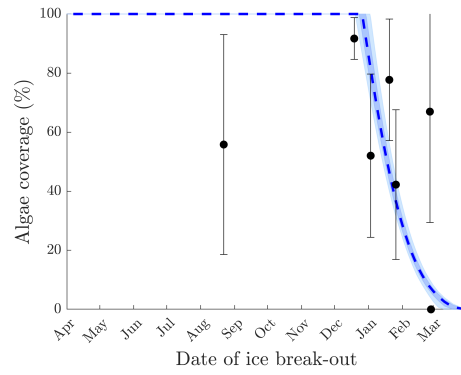
(b) Step Model, algae cover vs sea-ice break-out date



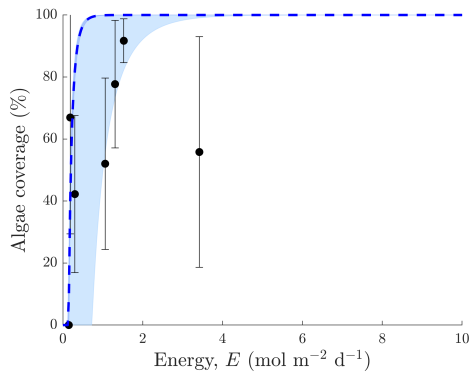
(c) Linear Model, algae cover vs light dose



(d) Linear Model, algae cover vs sea-ice break-out date



(e) Geometric Model, algae cover vs light dose



(f) Geometric Model, algae cover vs sea-ice break-out date

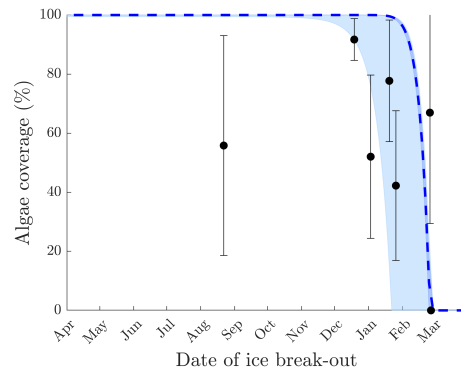


Figure S3.5: Model-data fits for top-oriented surfaces of boulders, interpreting the data as relative to the cumulative cover of nonabundant invertebrates and algae. (See caption of Figure 8 for further details.)

## S4. Parameter posterior distributions

The figures in this section show the marginal posterior distributions for the compensation irradiance  $E_c$ , saturation irradiance  $E_{\text{sat}}$  (Linear Model only), carrying capacity  $K$  (where the data was interpreted as absolute values only) and standard deviation  $\sigma$ . The  $x$ -axis bounds represent the chosen bounds for the prior distribution.

The marginal distributions for the compensation irradiance  $E_c$  (Figures S4.1 to S4.3) illustrates why the Step Model experienced much higher levels of uncertainty than the Linear Model and Geometric Model, and why it was unable to provide meaningful estimates of tipping points. The multimodality arising from the Step Model (seen in Figure S4.1b) is due to the limited number of sites at which sides of boulders were subjected to high annual light doses ( $\gtrsim 2 \text{ mol m}^{-2} \text{ d}^{-1}$ ); this issue was not present in the other two models tested.

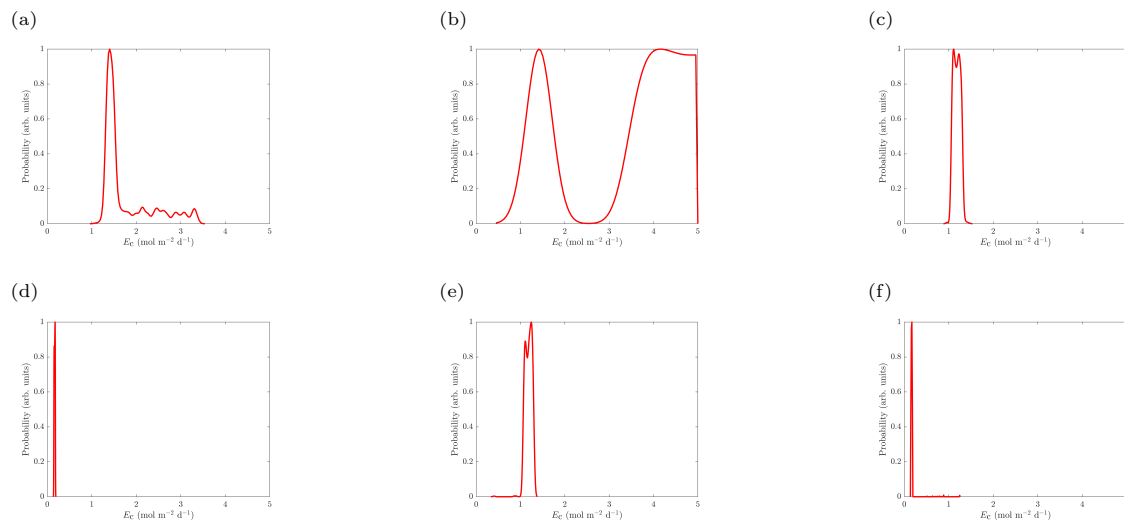


Figure S4.1: Marginal posterior distribution of the compensation irradiance  $E_c$  for the Step Model for the scenarios: (a) side data, absolute. (b) side data, relative to cumulative cover of algae and all invertebrates. (c) side data, relative to the cumulative cover of algae and nonabundant invertebrates. (d) top data, absolute. (e) top data, relative to cumulative cover of algae and all invertebrates. (f) top data, relative to cumulative cover of algae and nonabundant invertebrates.

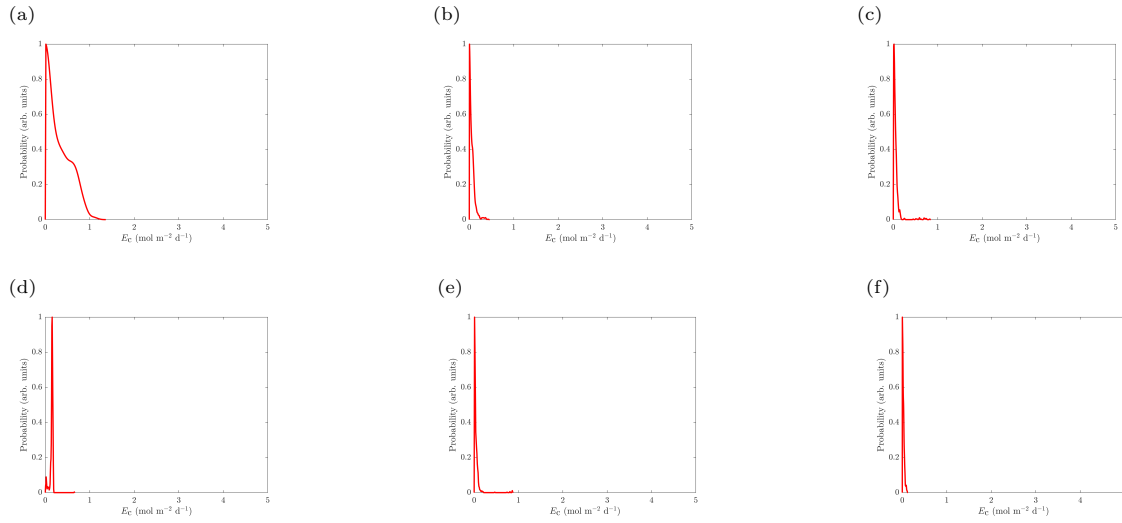


Figure S4.2: Marginal posterior distribution of the compensation irradiance  $E_c$  for the Linear Model for the scenarios: (a) side data, absolute. (b) side data, relative to cumulative cover of algae and all invertebrates. (c) side data, relative to the cumulative cover of algae and nonabundant invertebrates. (d) top data, absolute. (e) top data, relative to cumulative cover of algae and all invertebrates. (f) top data, relative to cumulative cover of algae and nonabundant invertebrates.

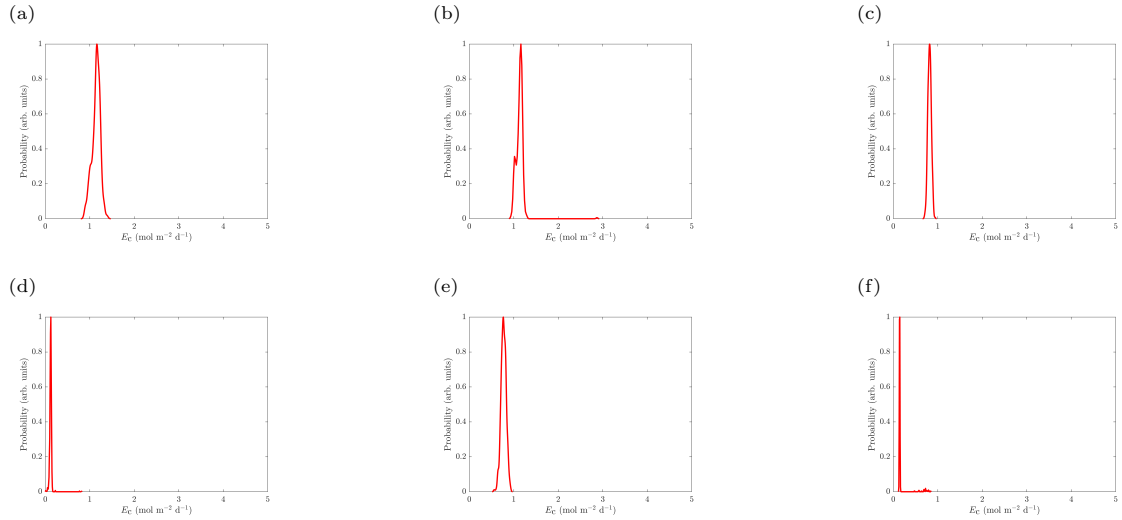


Figure S4.3: Marginal posterior distribution of the compensation irradiance  $E_c$  for the Geometric Model for the scenarios: (a) side data, absolute. (b) side data, relative to cumulative cover of algae and all invertebrates. (c) side data, relative to the cumulative cover of algae and nonabundant invertebrates. (d) top data, absolute. (e) top data, relative to cumulative cover of algae and all invertebrates. (f) top data, relative to cumulative cover of algae and nonabundant invertebrates.

The marginal posterior distributions for the saturation irradiance  $E_{\text{sat}}$  provides insight as to why

two scenarios resulted in a much higher uncertainty, reported in Table 3. Figure S4.4 shows that for data taken from the side-oriented surfaces of boulders, when the data is interpreted as either absolute values, or relative to the cumulative cover of algae and all invertebrates, the posterior marginal distributions span a wider range than the other scenarios.

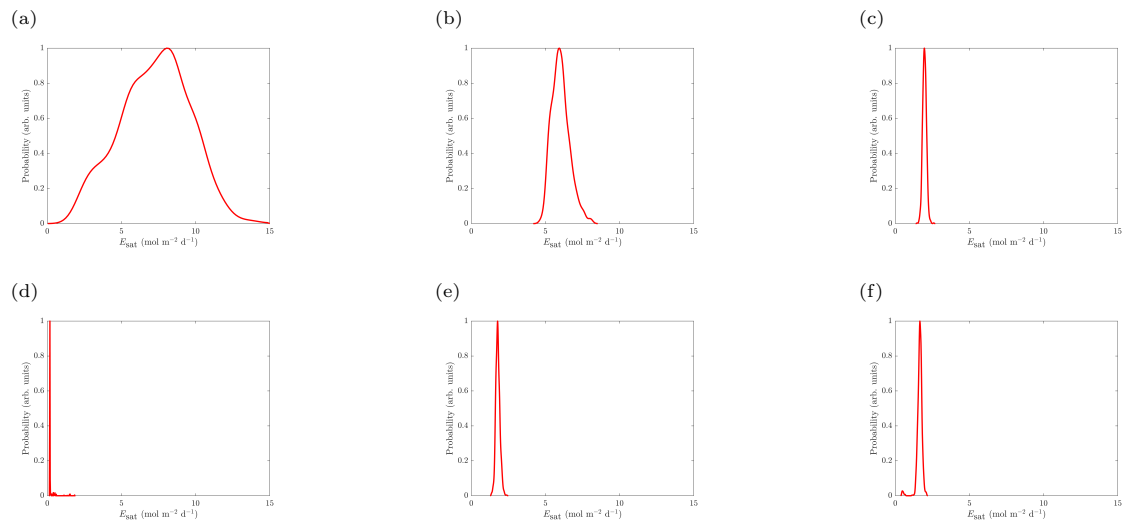


Figure S4.4: Marginal posterior distribution of the saturation irradiance  $E_{\text{sat}}$  for the Linear Model for the scenarios: (a) side data, absolute. (b) side data, relative to cumulative cover of algae and all invertebrates. (c) side data, relative to the cumulative cover of algae and nonabundant invertebrates. (d) top data, absolute. (e) top data, relative to cumulative cover of algae and all invertebrates. (f) top data, relative to cumulative cover of algae and nonabundant invertebrates.

The marginal posterior distributions for the carrying capacity  $K$  (Figure S4.5) show that predictions are generally well constrained, with only one model/scenario combination unable to predict a constrained estimate (Figure S4.5c), accounting for the higher uncertainty in that predicted value.

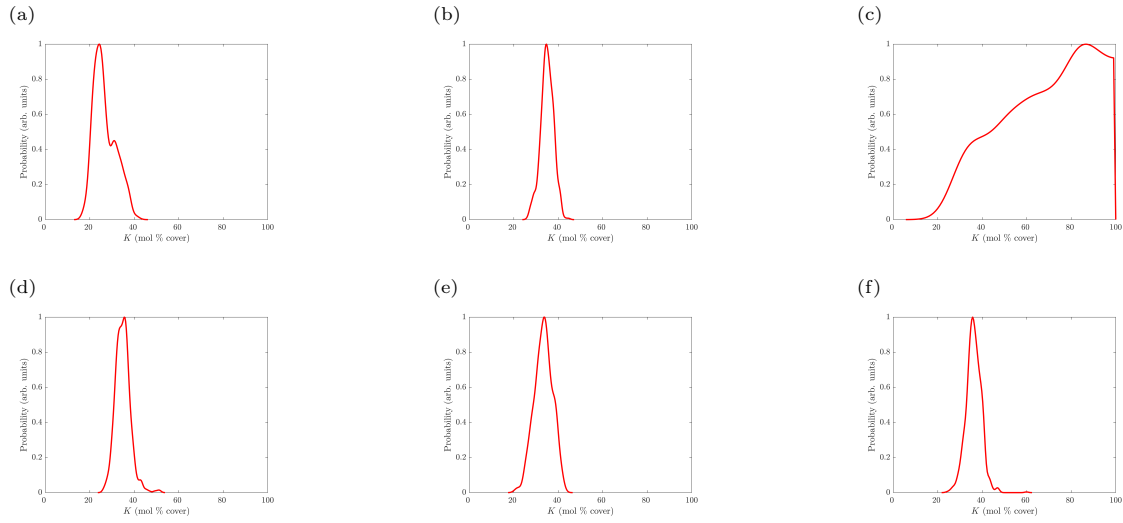


Figure S4.5: Marginal posterior distribution of the carrying capacity  $K$  for: (a) Step Model, side data, absolute. (b) Step Model, top data, absolute. (c) Linear Model, side data, absolute. (d) Linear Model, top data, absolute. (e) Geometric Model, side data, absolute. (f) Geometric Model, top data, absolute.

Posterior marginal distributions for the standard deviation  $\sigma$  (Figures S4.6 to S4.8) were consistently well-constrained.

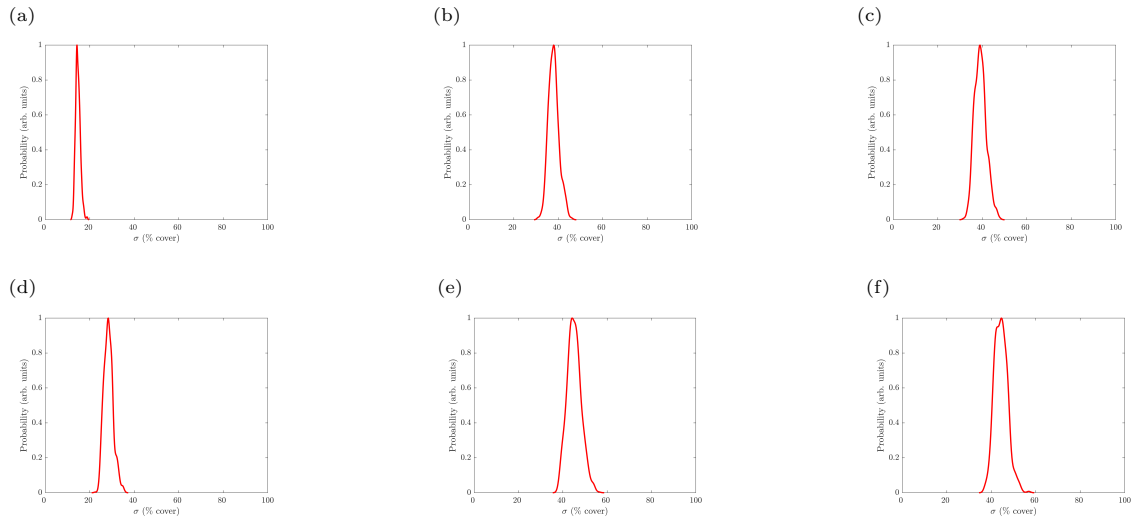


Figure S4.6: Marginal posterior distribution of the standard deviation  $\sigma$  for Step Model for the scenarios: (a) side data, absolute. (b) side data, relative to cumulative cover of algae and all invertebrates. (c) side data, relative to the cumulative cover of algae and nonabundant invertebrates. (d) top data, absolute. (e) top data, relative to cumulative cover of algae and all invertebrates. (f) top data, relative to cumulative cover of algae and nonabundant invertebrates.



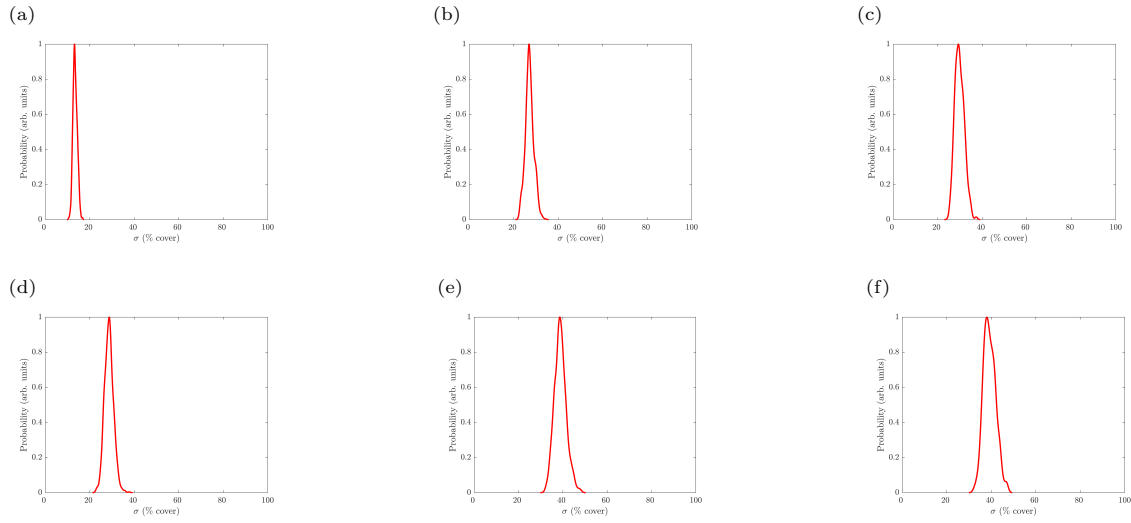


Figure S4.7: Marginal posterior distribution of the standard deviation  $\sigma$  for the Linear Model for the scenarios: (a) side data, absolute. (b) side data, relative to cumulative cover of algae and all invertebrates. (c) side data, relative to the cumulative cover of algae and nonabundant invertebrates. (d) top data, absolute. (e) top data, relative to cumulative cover of algae and all invertebrates. (f) top data, relative to cumulative cover of algae and nonabundant invertebrates.

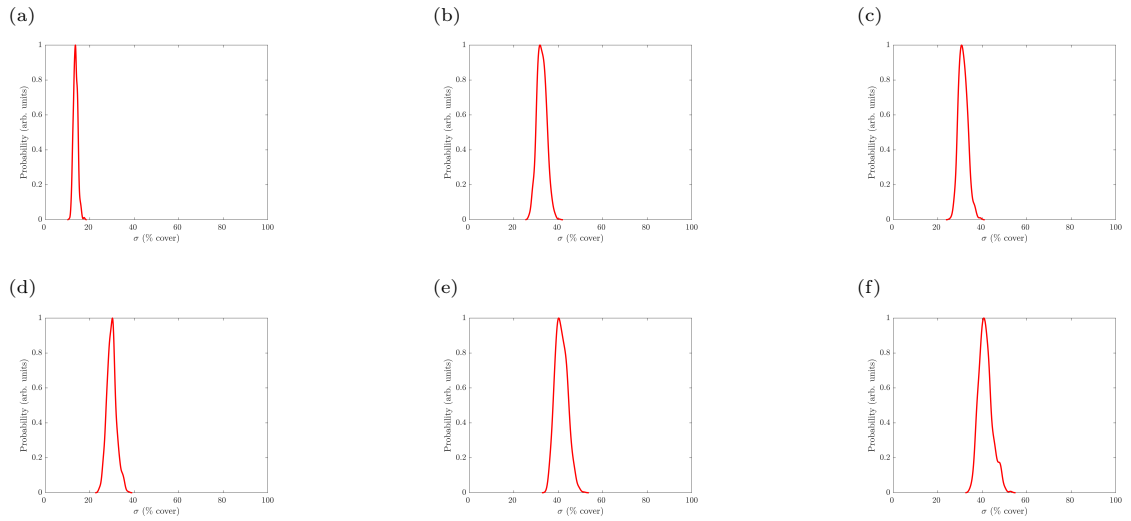


Figure S4.8: Marginal posterior distribution of the standard deviation  $\sigma$  for the Geometric Model for the scenarios: (a) side data, absolute. (b) side data, relative to cumulative cover of algae and all invertebrates. (c) side data, relative to the cumulative cover of algae and nonabundant invertebrates. (d) top data, absolute. (e) top data, relative to cumulative cover of algae and all invertebrates. (f) top data, relative to cumulative cover of algae and nonabundant invertebrates.

## References

Clark, G. F., Stark, J. S., Johnston, E. L., Runcie, J. W., Goldsworthy, P. M., Raymond, B., and Riddle, M. J. (2013). Light-driven tipping points in polar ecosystems. *Global Change Biology*, 19(12):3749–3761.